

Single-nucleus multiregion transcriptomic analysis of brain vasculature in Alzheimer's disease

Received: 15 February 2022

Accepted: 17 April 2023

Published online: 1 June 2023

 Check for updates

Na Sun^{1,2}, Leyla Anne Akay^{1,2,3,4}, Mitchell H. Murdock^{3,4}, Yongjin Park^{1,2,5,6}, Fabiola Galiana-Melendez^{3,4}, Adele Bubnys^{3,4}, Kyriaki Galani^{1,2}, Hansruedi Mathys^{3,4,7}, Xueqiao Jiang^{3,4}, Ayesha P. Ng^{3,4}, David A. Bennett⁸, Li-Huei Tsai^{1,2,3,4,9}✉ & Manolis Kellis^{1,2,9}✉

Cerebrovascular dysregulation is a hallmark of Alzheimer's disease (AD), but the changes that occur in specific cell types have not been fully characterized. Here, we profile single-nucleus transcriptomes in the human cerebrovasculature in six brain regions from 220 individuals with AD and 208 age-matched controls. We annotate 22,514 cerebrovascular cells, including 11 subtypes of endothelial, pericyte, smooth muscle, perivascular fibroblast and ependymal cells. We identify 2,676 differentially expressed genes in AD, including downregulation of *PDGFRB* in pericytes, and of *ABCBI* and *ATPIOA* in endothelial cells, and validate the downregulation of *SLC6A1* and upregulation of *APOD*, *INSR* and *COL4A1* in postmortem AD brain tissues. We detect vasculature, glial and neuronal coexpressed gene modules, suggesting coordinated neurovascular unit dysregulation in AD. Integration with AD genetics reveals 125 AD differentially expressed genes directly linked to AD-associated genetic variants. Lastly, we show that APOE4 genotype-associated differences are significantly enriched among AD-associated genes in capillary and venule endothelial cells, as well as subsets of pericytes and fibroblasts.

Blood–brain barrier (BBB) breakdown may be an early feature of Alzheimer's disease (AD), preceding dementia and neurodegeneration, thereby suggesting a critical role of neurovascular unit dysfunction in the progression of AD¹. This breakdown leads to the influx of toxic molecules, pathogens and cells from peripheral blood into the central nervous system, triggering inflammatory and immune responses².

The combination of single-nucleus RNA sequencing (snRNA-seq) technologies and vessel enrichment protocols has provided an atlas of

brain vasculature cell types in human and mouse^{3–5}. However, cell sorting and enrichment protocols can introduce technical biases in cell type composition. Thus, molecular characterization of human cerebrovascular cell types using sorting-free and enrichment-free methods is needed to understand the cellular basis of the neurovascular unit. Moreover, different brain regions possess cellular, morphological and functional differences in vasculature⁶. Understanding this molecular heterogeneity can provide insights into the unique vulnerabilities of different brain regions to disease.

¹MIT Computer Science and Artificial Intelligence Laboratory, Cambridge, MA, USA. ²Broad Institute of MIT and Harvard, Cambridge, MA, USA. ³Picower Institute for Learning and Memory, Massachusetts Institute of Technology, Cambridge, MA, USA. ⁴Department of Brain and Cognitive Sciences, Massachusetts Institute of Technology, Cambridge, MA, USA. ⁵Department of Pathology and Laboratory Medicine, Department of Statistics, University of British Columbia, Vancouver, British Columbia, Canada. ⁶Department of Molecular Oncology, BC Cancer, Vancouver, British Columbia, Canada. ⁷Department of Neurobiology, University of Pittsburgh School of Medicine, Pittsburgh, PA, USA. ⁸Rush Alzheimer's Disease Center, Rush University Medical Center, Chicago, IL, USA. ⁹These authors jointly supervised this work: Li-Huei Tsai, Manolis Kellis. ✉e-mail: lhtsai@mit.edu; manoli@mit.edu

In this study, we report an atlas of 22,514 transcriptomes of cerebrovascular single nuclei from six brain regions across 220 individuals with AD and 208 age-matched controls, covering 11 cell types. We find substantial proportional and transcriptional differences between brain regions, highlighting the regional heterogeneity of the BBB. We also find 2,676 cell type-specific differentially expressed genes (DEGs) in AD. Differential cell–cell communication analysis suggests the existence of mechanistic mediators of neurovascular unit dysregulation in AD. Integration with AD genetics reveals that approximately 37% of AD DEGs can be linked to AD-associated genetic variants. Lastly, we show that APOE4 genotype-associated differences are significantly enriched in subsets of endothelial cells, pericytes (PERs) and fibroblasts (FIBs). This underlies vascular dysregulation in APOE4-associated cognitive decline.

Results

Brain vasculature characterization across six brain regions

To characterize human cerebrovascular cells and their transcriptomic differences in AD, we profiled and analyzed the transcriptome of 22,514 single nuclei from 725 postmortem brain samples of 220 individuals with AD and 208 controls (Supplementary Table 1 and Supplementary Fig. 1a–c) across six brain regions: the prefrontal cortex (PFC) (area BA9); the hippocampus; the mid-temporal cortex; the angular gyrus; the entorhinal cortex; and the thalamus. We defined controls (individuals without AD) as individuals with little to no AD pathology, whereas cases (AD) included a spectrum of AD and cognition pathologies (Supplementary Fig. 1a and Methods). We annotated 11 vascular cell types, including three types of endothelial cells (marked by *FLT1* and *CLDN5*), two types of PERs (marked by *RGS5* and *PDGFRB*), two types of smooth muscle cells (SMCs) (marked by *ACTA2*), and three types of FIBs (marked by *COL3A1*) and ependymal (Epend) cells (marked by *TTR*) (Fig. 1a,b) using expression of canonical markers^{3,4} (Fig. 1c,d and Extended Data Fig. 1a). Consistent with two recent studies^{4,5}, we found distinct transcriptomic signatures of arterial (aEndo), capillary (cEndo) and venule (vEndo) endothelial cells, arterial (aSMC) and venule (vSMC) SMCs, showing specialized functions in different vessel types (Supplementary Tables 2 and 3 and Methods). The inclusion of Epend cells by our marker-based in silico cell sorting highlights the transcriptional commonalities of the cerebrospinal fluid and BBB. Integration with an independent vessel enrichment-based dataset⁵ confirmed the vascular cell types and subtypes we characterized (Extended Data Fig. 1b–e and Methods), suggesting that the technical difference between the two studies does not impact cell type identification at the single-cell level.

To gain insights into the gene regulatory mechanisms, we next predicted upstream regulators whose activities are associated with molecular function and cell identity. We found that the major cell types shared upstream regulators but still showed subtype specificity (Fig. 1e). Some of the top regulators of cell identity showed high enrichment in endothelial cells, such as *CTNGB1*, which is associated with maintenance of BBB integrity through endothelial β -catenin signaling⁷. For PERs, we found enrichment of *BACH1*, which is consistent with its transcriptional regulation of pro-angiogenic activity via modulating the expression of angiopoietin-1 (ref. 8).

We next evaluated whether vascular cells show differences in abundance across brain regions and phenotypic variables. We found significantly higher proportions of FIBs and lower proportions of PERs and cEndo cells in the entorhinal cortex, hippocampus and thalamus (Fig. 1f,g and Extended Data Fig. 2a; false discovery rate (FDR) < 0.05 by Wilcoxon rank-sum test), which is consistent with the paucity of small vessels in the brain⁹. In contrast to these regional differences, we observed that vascular cell fractions did not differ according to sex, AD pathology, age or postmortem interval (PMI) (Extended Data Fig. 2b–h; FDR < 0.05 by Wilcoxon rank-sum test). We also found no statistically significant differences in vascular fractions between this

study and the other datasets^{10,11,12} (Supplementary Fig. 2a), suggesting that the cell capture rate is similar across different studies when there is no enrichment for vascular cells. We also found no significant correlation between the number of detected genes or captured cells and cell fraction (Supplementary Fig. 2b–e). However, we found a significantly higher proportion of FIBs (FIB1 and FIB2) in this study in both hippocampus and PFC (Extended Data Fig. 2i,j and Methods; FDR < 0.05 by Wilcoxon rank-sum test) compared with a vessel enrichment dataset, suggesting that capturing of perivascular-like FIBs might be sensitive to the techniques used.

In addition, we found that vasculature cells showed extensive gene expression differences between brain regions, with 1,745 DEGs between brain regions (brDEGs) in the six cell types that had enough cells from each region to be included in this analysis, showing many region-specific pathway enrichments and highlighting the regional heterogeneity of the BBB (Extended Data Fig. 3, Supplementary Tables 4 and 5 and Methods).

Cell type-specific brain vasculature changes in AD

To investigate the association between vascular gene expression and AD, we identified 2,676 AD DEGs (adDEGs) between individuals with AD and controls by combining the cells from different brain regions across all cell types (306 on average for each cell type) using a single-cell-based method with consideration of covariates. This number of adDEGs was significantly more than expected by permutation analysis (t -test, $P = 0.007$; Extended Data Fig. 4a and Methods) and was confirmed at the pseudobulk level (Extended Data Fig. 4b and Methods). Of these, 2,142 were unique to only one cell type, highlighting the cell type specificity of adDEGs (Fig. 2a,b and Supplementary Table 6). Notably, cEndo cells had the highest number of adDEGs, which we recapitulated through a downsampling analysis (Extended Data Fig. 4c), highlighting the importance of transcriptional differences in cEndo functions associated with AD pathology (Fig. 2a).

Among the top adDEGs are cell junction-associated and adhesion-associated genes including *APOD*, *PECAMI1* and *COLEC12*; transporters including *SLC38A2*, *SLC2A1* and *SLC6A1*; and sterol import-associated genes including *RORA*, *PRKAA2* and *PPARG* (Fig. 2c), indicating that these fundamental functions of vascular cell types may be dysregulated in AD. As expected, we detected downregulation of *PDGFRB* in the PERs of the AD samples (Fig. 2c), alluding to PER injury and dysfunction of BBB integrity in AD¹³. We also found that *ABCBI*, which encodes P-glycoprotein, was significantly downregulated in cEndo cells (Fig. 2c), which is consistent with its role in amyloid- β clearance in the neurovascular unit in AD¹⁴ and the observations that individuals with early AD develop widespread reductions in P-glycoprotein BBB function in multiple brain regions¹⁵.

To evaluate if these adDEGs are consistent across the six brain regions, we identified adDEGs for each region and found significant overlap of adDEGs between regions in six cell types that had enough cells for analysis (Extended Data Fig. 4d and Methods). Notably, the three cell types with the highest number of cells (cEndo, PER1 and FIB1) showed the greatest overlap. Further research with more cells from each brain region would improve the power to detect region-specific transcriptional changes in AD.

Gene Ontology (GO) enrichment analysis of adDEGs showed that multiple broad functional pathways were shared across cell types, suggesting that transcriptional changes in AD converge to common functionalities at the pathway level; however, multiple pathways were more cell type-specific (Fig. 2d–g, Extended Data Fig. 5a,b, Supplementary Table 7 and Methods). For example, we found that the immune response (cytokine, interleukin-17 signaling and inflammatory response) was broadly enriched in FIB, endothelial and PER upregulated adDEGs, suggesting a potential inflammatory microenvironment in individuals with AD. We found that synaptic transmission, cytoskeleton remodeling and contraction were especially enriched in PER downregulated adDEGs,

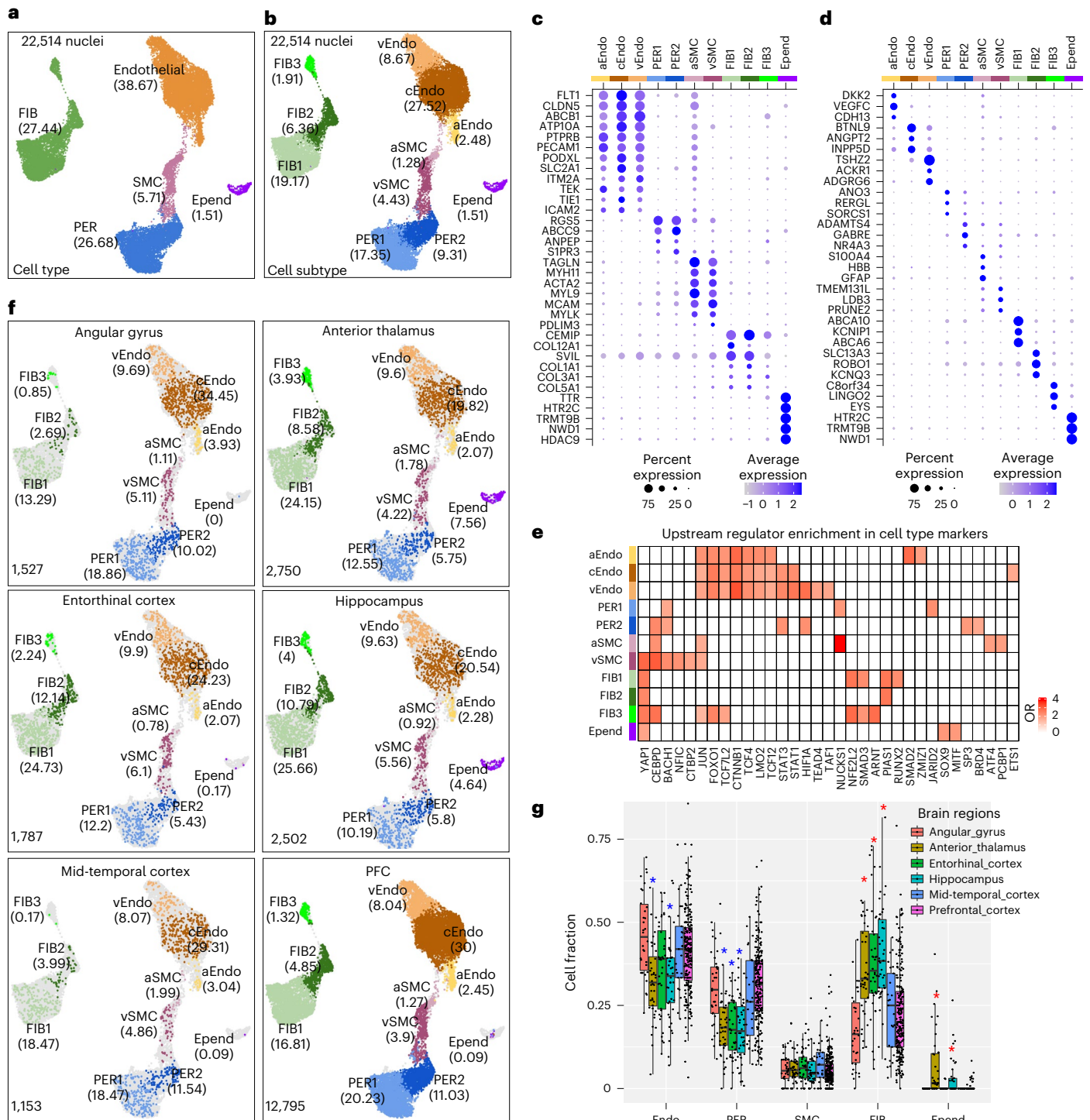


Fig. 1 | Brain vasculature characterization across six brain regions.

a, b, Uniform manifold approximation and projection (UMAP) of 22,514 in silico-sorted brain vascular nuclei from postmortem tissues labeled according to cell type (**a**) and subtype (**b**); the percentage of cells in each cell type is shown. **c, d**, Top 5 markers for vascular cell types (**c**) and subtypes (**d**). The size of the dots represents the percentage of cells with expression. The color of the dots represents the scaled average expression level. **e**, Heatmap showing the enrichment of upstream regulators for cell subtype markers. The OR represents the enrichment. The Enrichr package in R was based on three libraries, including TRANSFAC and JASPAR, ChEA and ENCODE TF. Chromatin immunoprecipitation followed by sequencing (ChIP-seq) data were used to predict upstream

regulators (proportion test, adjusted $P < 0.05$ as the cutoff). Only regulators with significantly high expression in the corresponding cell types are shown. **f**, UMAP of vascular nuclei for each brain region. The percentage of cells in each cell type is shown. **g**, Distribution of cell fraction across six brain regions in major cell types. The asterisks represent the significance of cell types enriched (red asterisks) or depleted (blue asterisks) in specific regions compared to the overall fraction using a two-sided Wilcoxon rank-sum test (adjusted $P < 0.05$). $n = 409$ in the PFC; 47 in the angular gyrus, mid-temporal cortex and thalamus; 45 in the entorhinal cortex; and 84 in the hippocampus. The box starts in the first quantile (25%) and ends in the third (75%). The line inside the box represents the median. The two whiskers without outliers represent the maximum and minimum.

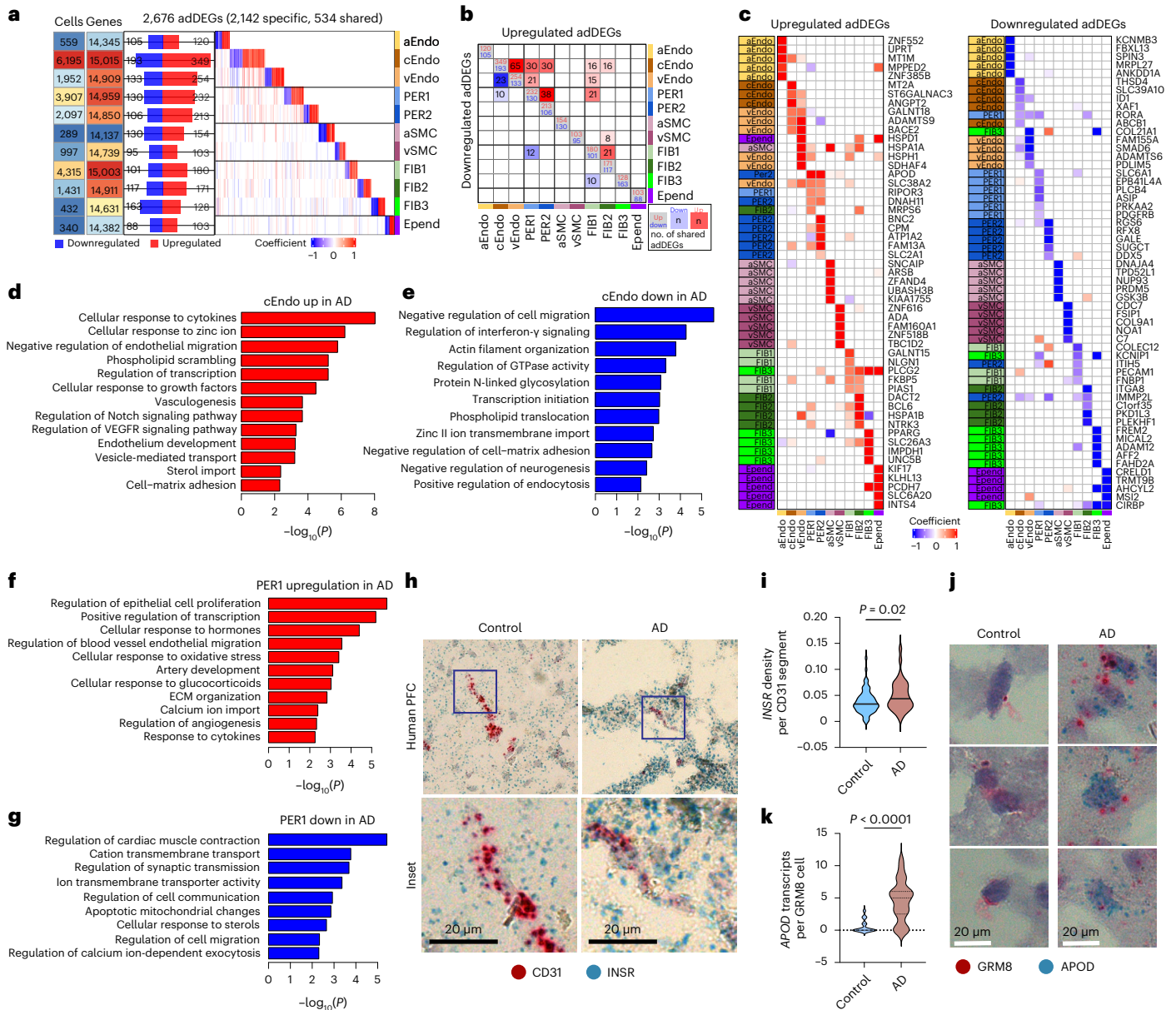


Fig. 2 | Cell type-specific brain vasculature changes in AD. **a**, Overview of adDEGs in each cell type. Left to right, Numbers of cells and expressed genes in each cell type, number of downregulated and upregulated adDEGs in AD and heatmap with each gene shown in the column and each cell type shown in the row. **b**, The number and significance of adDEG overlap between cell types in both directions (upper triangle: upregulated adDEGs; lower triangle: downregulated adDEGs). The blocks shaded in blue or red represent significant overlap (the darker, the more significant). **c**, Top 5 upregulated and downregulated adDEGs in AD in each cell type. The highest effect size for each gene is colored according to the cell type in the left column of the heatmap. **d–g**, Enriched GO biological

processes in upregulated (**d**) and downregulated (**e**) adDEGs in cEndo cells, and upregulated (**f**) and downregulated (**g**) adDEGs in PER1. The Enrichr package in R was used to perform GO enrichment (proportion test, adjusted $P < 0.05$ as the cutoff). **h, i**, Representative images (**h**) and quantification (**i**) of *INSR* transcripts in *CD31*⁺ endothelial cells from control and AD PFC tissues by RNA in situ hybridization (t -test, adjusted $P < 0.05$). $n = 4$ for individuals with AD and $n = 4$ for individuals without AD. **j, k**, Representative images (**j**) and quantification (**k**) of *APOD* transcripts in *GRM8*⁺ PERs from control and AD PFC tissues by RNA in situ hybridization (t -test, adjusted $P < 0.05$). $n = 4$ for individuals with AD and $n = 4$ for individuals without AD.

which is consistent with loss of neuronal signal sensing and impaired blood flow control in AD PERs^{16,17}.

Notably, our analysis revealed that insulin signaling genes were dysregulated in AD across multiple cell types (cEndo, PER, FIB, SMC and Epend; Extended Data Fig. 4d). To validate our snRNA-based observation that *INSR*, which encodes the insulin cognate receptor, was upregulated in endothelial cells from individuals with AD ($P < 0.0019$), we performed RNA in situ hybridization (Methods)¹⁸ and found that *CD31*⁺ vascular segments harbored a higher density of *INSR* transcripts in individuals with AD. We found that a subset of *CD31*⁺ endothelial

cells from the brains of individuals with AD possessed higher density of *INSR*⁺ punctae (Fig. 2h,i). These suggest that subsets of endothelial cells may express differential levels of the insulin receptor, potentially making cells more or less sensitive to insulin signaling. We also observed that *APOD*, which encodes a component of high-density lipoprotein (HDL), was upregulated in AD mural cells (particularly PERs, $P < 3.9 \times 10^{-12}$; Fig. 2c), which is consistent with the previously reported upregulation of *APOD* in AD¹⁹. To validate upregulation in AD PERs, we quantified *APOD* transcript abundance in *GRM8*-labeled cells (a previously validated marker for PERs⁴ that is not significantly differentially

expressed in AD) using in situ hybridization and observed higher *APOD* expression in *GRM8*⁺ PERs in individuals with AD (Fig. 2j,k). We did not use *PDGFRB* as a PER marker because it is downregulated in AD (Fig. 2c). The functional consequences of *APOD* upregulation in PERs, and the impact on lipid transport within the neurovascular unit, will form the basis of future studies. Additionally, we validated the downregulation of *SLC6A1* in AD PERs (*ABCC9* as the marker) using RNAscope (Extended Data Fig. 6a,b) and upregulation of *COL4A1* (encoding type IV collagen) in the endothelial cells of individuals with AD at the protein level using immunohistochemistry (IHC) staining (Extended Data Fig. 6c,d).

Our results show no significant change in vascular cell proportions between individuals with and without AD (Extended Data Fig. 2d–f); in fact, a modest but non-significant high in the median number of cEndo cells and PERs in individuals with AD was observed, which was consistent with an observed higher proportion of endothelial cells in AD in two recent studies^{10,20} that also did not rely on any vessel enrichment protocols. However, we found that several of our downregulated adDEGs were cell type marker genes, including *PDGFRB* (PERs), and *ABCB1*, *ATP10A*, *PTPRB* and *TEK* (cEndo cells), suggesting potential loss of vascular cell type integrity in AD. Such loss of vascular integrity, and decreased expression of cell type-specific markers, could result in an apparent decrease in vascular cell proportions in studies that rely on enrichment protocols.

Upstream regulators of DEGs in AD

To gain insights into the transcriptional regulatory mechanisms, we inferred upstream regulators of adDEGs, including transcription factors (TFs), cofactors and epigenetic enzymes (Methods and Supplementary Table 8). We identified 118 upstream regulators of upregulated adDEGs (Fig. 3a) and 81 regulators of downregulated adDEGs (Fig. 3b), of which 66 targeted both upregulated and downregulated adDEGs across cell types. Seventeen of these 133 regulators were significant adDEGs corresponding to the differential direction of their targets.

We next grouped these regulators into coregulatory modules (defined as tfModules) for each cell type (Fig. 3c and Extended Data Fig. 7) when regulators showed significant sharing of target genes. Focusing on upregulated adDEGs in cEndo, which showed the largest number of adDEGs and upstream regulators, we identified seven regulatory tfModules (Fig. 3d) encompassing 38 regulators, and 11 regulators outside the tfModules. Although our tfModules were discovered solely based on their shared target genes, five of seven modules were additionally supported by independent experimental evidence of physical interactions²¹ (Fig. 3e), which were significantly enriched by a permutation test (FDR < 0.05; Methods). Moreover, regulators in the same tfModule frequently had related functions; for example, module M1 regulators had roles in vEndo cell function, growth and adhesion^{22–30}.

Within each tfModule, regulators varied in their number of target genes, their differential expression in AD and the differential expression

of their targets (Fig. 3d, left). For example, in tfModule 4, *MECOM*, which has been linked to high expression in vEndo cells and AD association³¹, showed a 1.37-fold upregulation in AD ($P = 8.8 \times 10^{-6}$) and 53 adDEG targets, with 100% of those targets upregulated in AD. In tfModule 6 (KLF and SMAD family), *KLF4*, which has been linked to anti-inflammatory properties in endothelial cells³², showed a 1.21-fold downregulation in AD ($P = 8.2 \times 10^{-4}$) and 47 (100% upregulated) adDEG targets, suggesting activation of an inflammatory response in AD. Not all regulators in each tfModule were DEGs, suggesting that some regulators may act through collaboration with differentially expressed regulators; for example, *STAT3* and *EP300* are significant adDEGs in module M1, but *JUN*, *JUND* and *GATA2* are not.

We used these tfModules to partition their target adDEGs into subgroups mediated by distinct combinations of tfModules (Methods). For cEndo upregulated adDEGs, we found groups targeted by a single tfModule (for example, G4, G5, G6) and other groups targeted by multiple tfModules (for example, G1, G2) (Fig. 3f), with distinct enrichment in common functional categories (Fig. 3g). For example, tfModule 2 (the chromatin modulators *RAD21*, *CTCF*, *SMC3*) targeted 58% of upregulated adDEGs (groups G1–G4), which is consistent with the known role of these regulators on chromatin structure maintenance³³. Conversely, adDEGs in G1 were targeted by regulators from most tfModules (M1–M4, M6) and were significantly enriched in cytokine response, cell adhesion and transcription regulation. Genes in several groups (G3, G7, G8) were enriched in the repression of endothelial cell proliferation and apoptotic signaling pathways, suggesting an endothelial injury response in AD, which is consistent with BBB breakdown.

Dynamics of cell–cell communication in AD

We next sought to understand the mechanistic basis of vascular communication with glia or neurons in the neurovascular unit and how this communication is altered in AD. We predicted bidirectional cell–cell communication between vascular and neuronal or glial cells using covariation analysis of gene modules (defined as degModules) across 409 individuals (Extended Data Fig. 8a and Methods). We identified 301 upregulated interactions in AD, where both interacting degModules showed upregulation in AD, and conversely 276 downregulated interactions in AD, where one or both interacting degModules showed decreased expression in AD (Fig. 4a,b and Supplementary Table 9). We found that the communication from PER1 and cEndo cells to neurons, microglia and astrocytes dominated the increased cell–cell interactions in AD, while communication from astrocytes and neurons to cEndo cells and FIB1s were mainly decreased in AD.

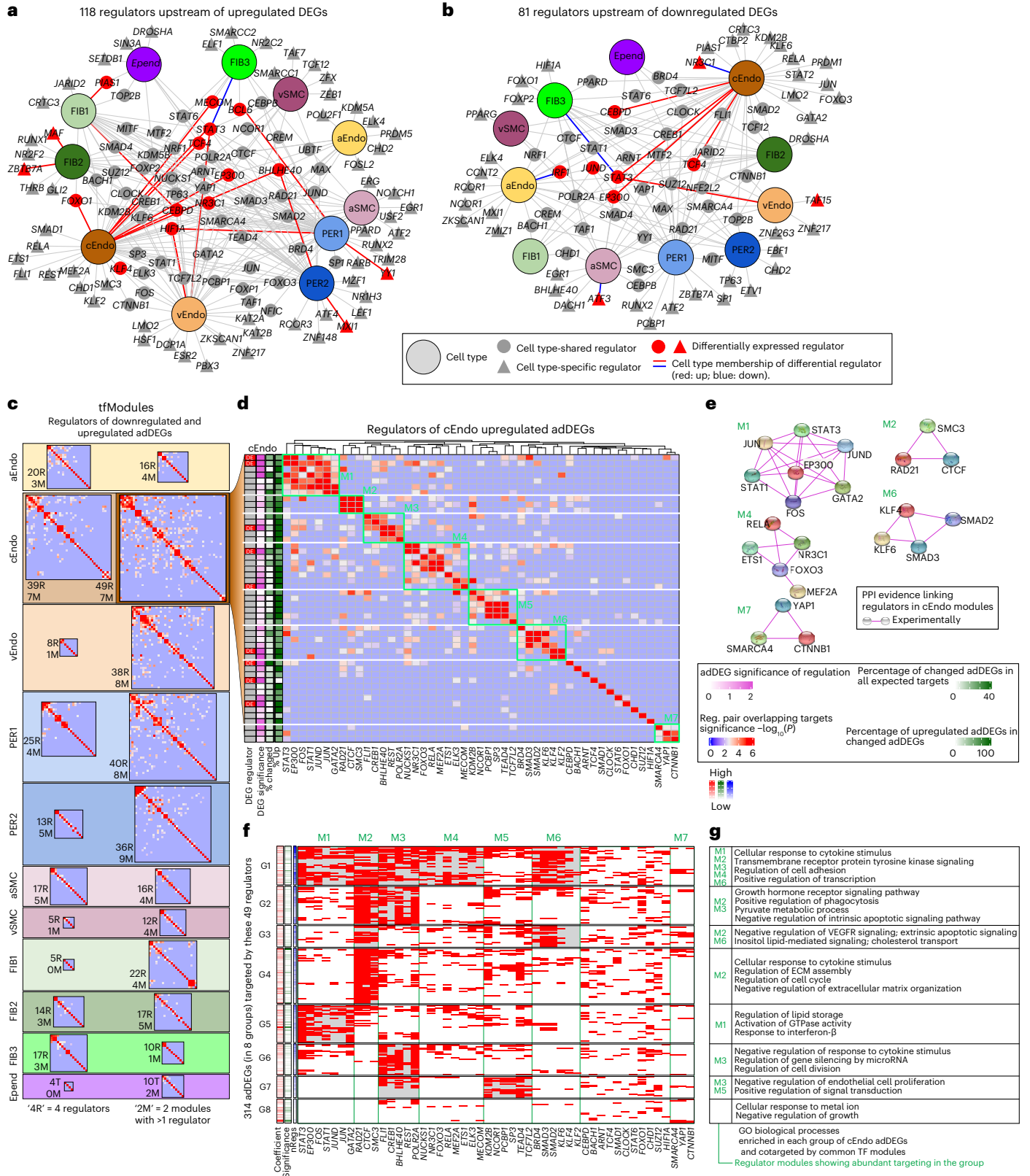
To characterize the ligand–receptor signaling pathways for this differential cell–cell communication, we aggregated individual interactions mediated by the same ligand–receptor pair and classified the ligand–receptor pairs into 62 signaling pathways based on the Kyoto Encyclopedia of Genes and Genomes, ligand family and receptor family annotations (Methods). The signaling pathways mediated by transforming growth factor- β (TGF β), secreted phosphoprotein 1 (SPP1),

Fig. 3 | Upstream regulators of DEGs in AD. **a, b**, Regulator–cell type networks in upregulated (**a**) and downregulated (**b**) adDEGs. Enrichr was used to predict regulators (proportion test, adjusted $P < 0.05$ as the cutoff). The large nodes represent cell types. Triangular nodes represent cell type-specific regulators. Gray nodes represent regulators with expression but not differentially expressed. Red nodes represent differentially expressed regulators. The red edges represent the corresponding differentially expressed regulators in relevant cell types. **c**, Overview of heatmaps that show coregulatory tfModules for all adDEGs sets (upregulated and downregulated for each cell type). For each cell type, two heatmaps show the tfModules (upregulated and downregulated adDEGs). The size of each heatmap reflects the number of regulators. The values in the heatmap were $-\log_{10}(P)$ -transformed to represent the significance of overlapping targets between regulators as in **d**. A Fisher's exact test was used (adjusted $P < 0.05$ as the cutoff). **d**, Coregulatory modules of upregulated adDEGs in

cEndo cells. Seven modules are boxed in green. The values in the heatmap are the significance of overlapping targets between regulators ($-\log_{10}(P)$) as in **c**. Left, Column 1: the regulator is differentially expressed; column 2: differential significance; column 3: percentage of targeted adDEGs in all targets of each regulator and percentage of targeted upregulated adDEGs in all targeted adDEGs. **e**, Physical protein–protein interaction networks for five of seven coregulatory modules. **f**, Heatmap showing the eight adDEG groups that were targeted by the regulators shown in **d**. Red indicates that a gene in a row is targeted by the regulator in the column. The blocks shaded gray highlight the regulation of specific coregulatory modules on the gene group. Left, Column 1: effect size of adDEGs; column 2: differential significance; column 3: number of regulators. **g**, Enriched GO biological processes of the genes in each group in **f**. The left column summarizes the coregulatory modules that could regulate the gene group. Enrichr was used (proportion test, adjusted $P < 0.05$ as the cutoff).

bone morphogenetic protein (BMP), angiopoietin-like (ANGPTL) and interleukin-6 (IL-6) were significantly overrepresented in AD-increased interactions, whereas collagen and laminin, the major extracellular matrix (ECM) proteins forming the basement membrane of the BBB³⁴, were overrepresented for AD-decreased interactions (Fig. 4c,d, Supplementary Table 9 and Methods), suggesting disruption of the BBB structure in AD.

We performed a permutation test (adjusted $P < 0.01$; Extended Data Fig. 8b and Methods) and found that most bidirectional cell–cell interaction changes in AD for each pair of cell types were significant, suggesting that the dysregulated genes in AD are highly related to multicellular interactions. We next separated the bidirectional AD differential cell–cell interactions into forward and reverse directions for each pair of cell types and quantified them. Interactions between cEndo



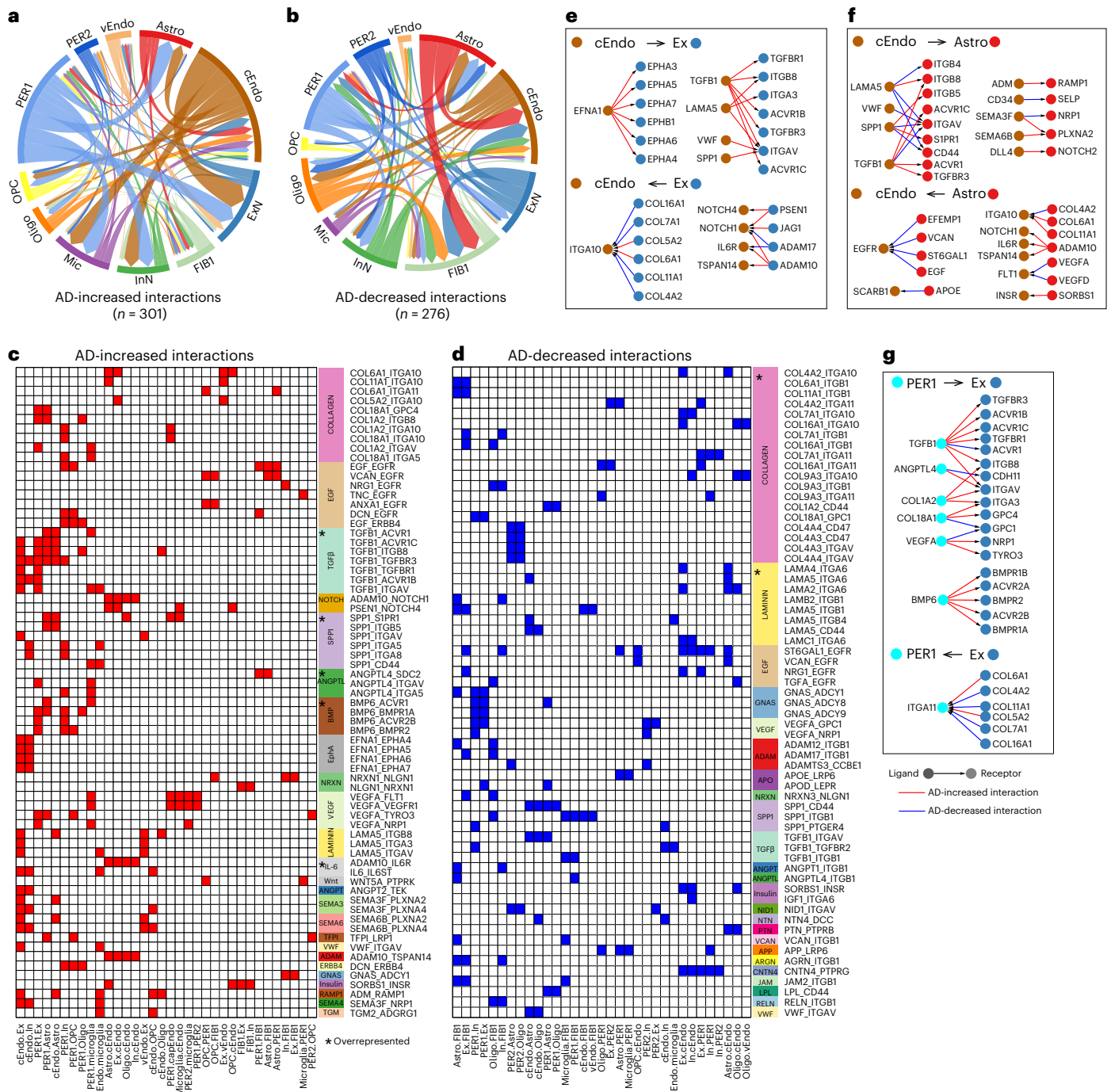


Fig. 4 | Dynamics of cell–cell communication between vascular cell types and neuron and glial cells in AD. **a, b**, Summary of increased (**a**) and decreased (**b**) interactions in AD mediated by ligand–receptor signaling between vascular cell types, and neuron, glial and microglial cell types in AD. The arrow represents the direction of the cell–cell interactions. The width of the edge reflects the number of interactions (the number of ligand–receptor pairs) between two cell types. **c, d**, Ligand–receptor pairs (row) in each pair of cell types (column) for increased (**c**) and decreased (**d**) interactions in AD. The signaling pathway is shown on the

right of the heatmap. The asterisk in the signaling pathway column indicates that the signaling pathway was significantly overrepresented (two-sided Fisher’s exact test, $P < 0.01$ as the cutoff). VEGF, vascular endothelial growth factor. **e–g**, Ligand–receptor networks in three pairs of interacting cell types: cEndo–Ex (**e**), cEndo–Astro (**f**) and PER1–Ex (**g**). Ligand–receptor interactions with direction are shown in the network. The color of the nodes represents the cell type. The red edges represent AD-increased interactions, whereas the blue edges represent AD-decreased interactions.

and PER1 cells, and excitatory neurons and astrocytes, showed the most interactions (Extended Data Fig. 8c, d). We then built ligand–receptor networks for the three cell–cell pairs with the largest number of interactions (cEndo–Ex, cEndo–Astro and PER1–Ex) to highlight specific ligand–receptor signaling pathways (Fig. 4e–g). For example, *TGFBI*, which exacerbates BBB permeability and regulates PER inflammatory

response^{35,36}, was highly expressed in capillary cell types in AD (cEndo and PER1) and mediated communication with excitatory neurons (Fig. 4e, g). *BMP6* mediates the AD-increased interactions between PERs (PER1) and excitatory neurons (Ex), suggesting that its function in PER governing impaired neurogenesis in AD³⁷. The AD-decreased interactions between astrocyte and cEndo cells mediated by epidermal

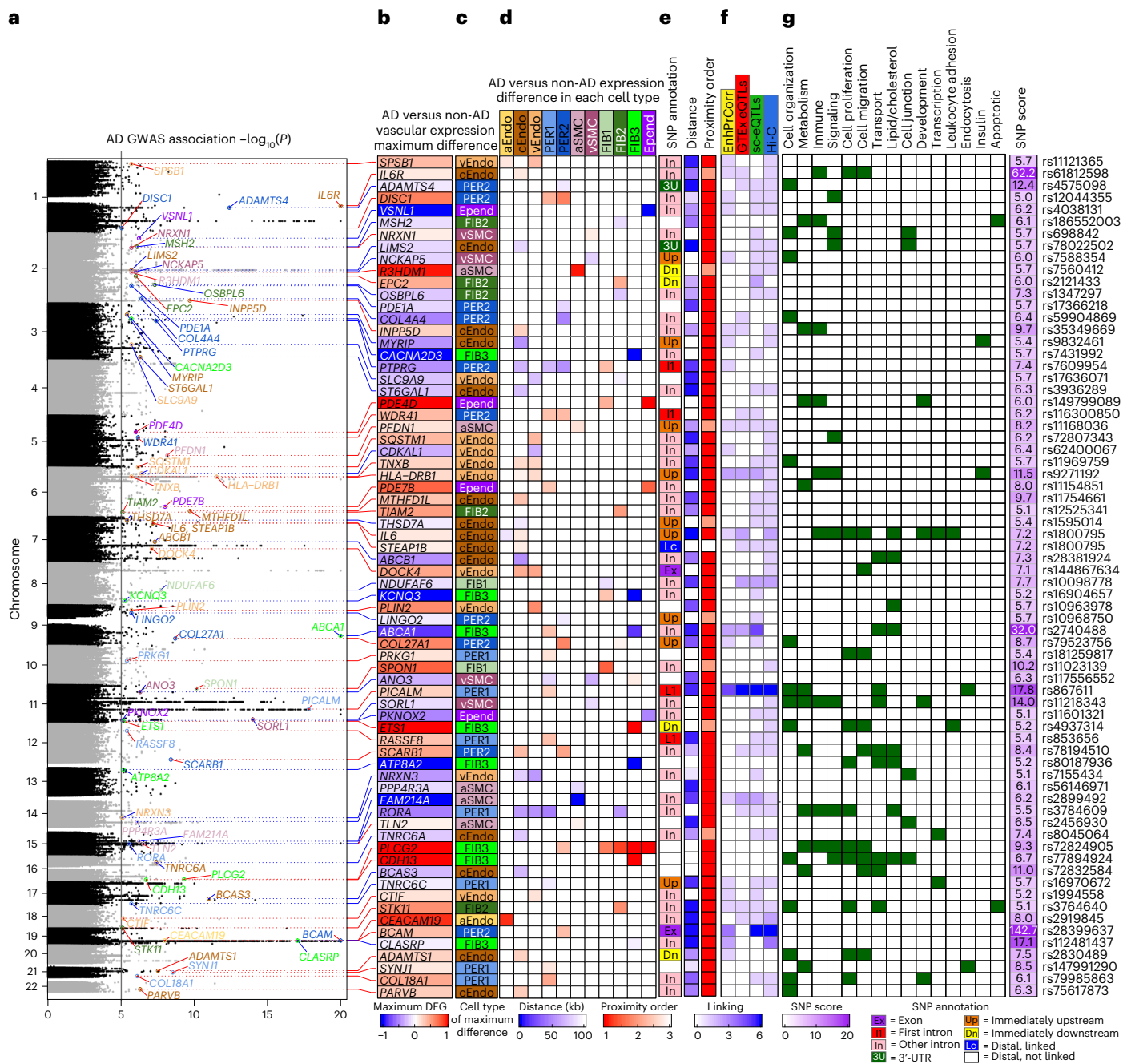


Fig. 5 | AD GWAS loci directly linked to brain vascular adDEGs. a–g, Direct (*cis*) regulated adDEGs according to AD-associated variants. The AD GWAS loci associated with significant adDEGs are shown. **a,b,** Gene names with the maximum effect size for a given AD GWAS locus are labeled on the plot. The color of the lines connecting the gene names in **a,b** and the shade of the box in the heatmap in column **b** indicate the direction of regulation in AD. **c,** Cell type in which the largest differential expression occurs. **d,** Heatmap showing differential expression across all cell types represented by effect size. **e,** Left column,

Genomic annotation for the single-nucleotide polymorphisms (SNPs) of the adDEGs. Middle column, Heatmap of the distance between variant and adDEG transcription start site (TSS) in kb. Right column, adDEG ranking among all associated genes of the specific variant in terms of proximity. **f,** Heatmap showing four pieces of linking evidence; values represent the number of appearances in the used datasets. **g,** Heatmap highlighting the enriched functions of adDEGs. The rightmost column shows the SNP score represented by $-\log_{10}(P)$ of the variants in AD.

growth factor (EGF) signaling pathways suggested inhibition of cEndo proliferation in AD³⁸ (Fig. 4f).

AD genome-wide association study loci are linked to brain vascular adDEGs

We next sought to gain an insight into how AD risk loci may lead to vasculature breakdown at the molecular level. We integrated AD-associated loci from genome-wide association studies

(GWAS)^{39–41} with our adDEGs (Fig. 5a) to predict their candidate target genes and directionality of effect (upregulated or downregulated in AD) (Fig. 5b), their cell types of action (Fig. 5c,d) and the direct (Fig. 5a–g) or indirect (Fig. 6) mechanisms through which they can lead to vascular gene expression changes (Extended Data Fig. 9a).

First, we focused on direct regulation of vascular adDEGs by nearby genetic variants (*cis*-regulation) and found 197 AD-associated variants in 113 loci^{42,43} ($P < 10^{-5}$) (Fig. 5a) proximal to 125 vascular adDEGs

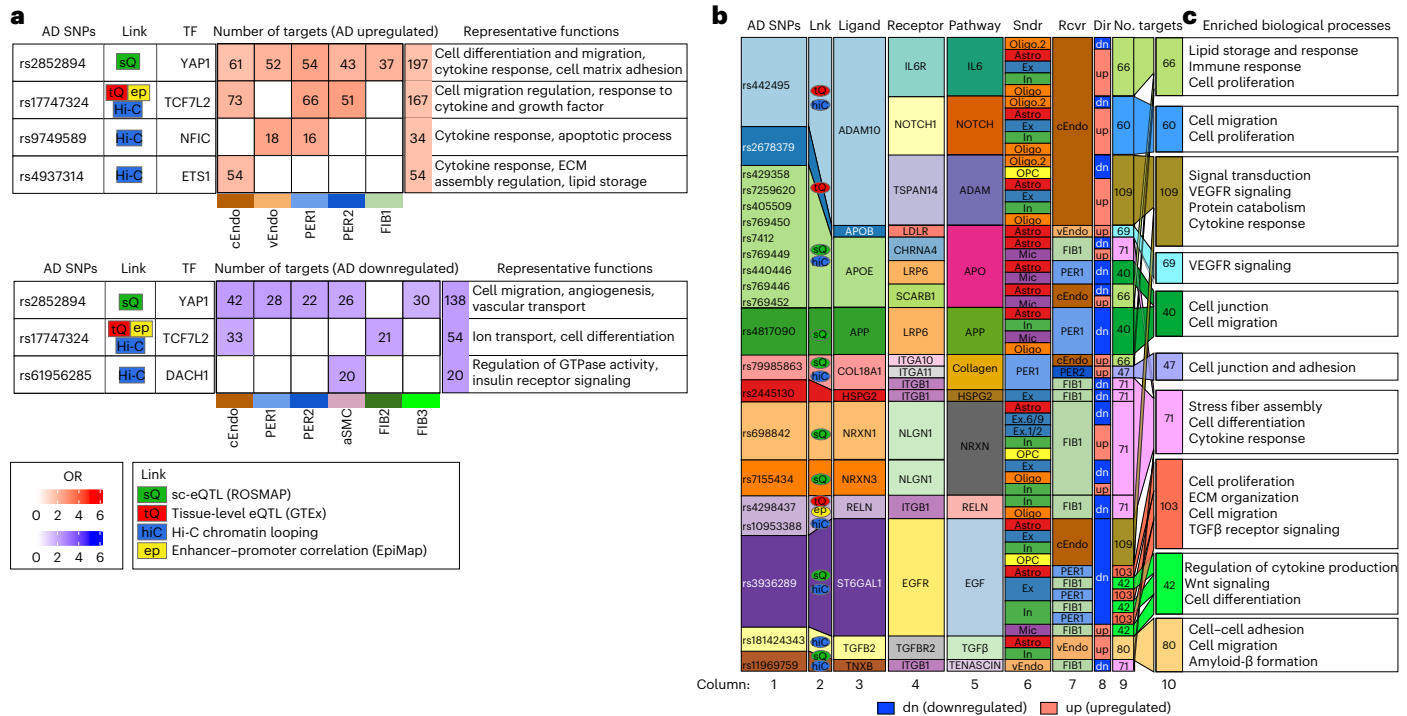


Fig. 6 | AD GWAS loci are indirectly linked to brain vascular adDEGs.

a, Summary of AD-associated TFs: AD variants; linking evidence; TFs; number of targets in adDEGs for each cell type and summation in all cell types; and representative functions of these targets. The color scale for the OR in red and blue refers to the enrichment of upregulated and downregulated adDEGs in the regulator’s targets. **b**, Summary of AD-associated ligands: AD variants; linking evidence (Lnk); ligands; receptors; signaling pathway; sender cell type; receiver cell type; differential direction (Dir) in AD; and number of targeted

adDEGs. The colors are matched to the columns of AD variants, linking evidence, and ligands to show the correspondence between AD variants and associated ligands. The colors of the sender (Sndr) and receiver (Rcvr) cell types match the cell types shown in Fig. 5c,d. The columns are aligned horizontally to show the correspondence. **c**, The enriched biological processes of the targets shown in **b** and the targets involved in the specific function. Enrichr in R was used to perform GO enrichment (proportion test, adjusted $P < 0.05$ as the cutoff).

(Fig. 5b and Supplementary Table 10) that show cell type-specific expression alterations (Fig. 5c,d). Most adDEGs harbored AD-associated variants within their introns (54.3%) or immediately upstream or downstream with no intervening gene (7.13%) (Fig. 5e), or were linked based on distinct evidence (Fig. 5f and Methods). These AD-associated adDEGs were enriched in multiple processes, including cholesterol transport, regulation of endothelial cell migration and IL-6-mediated signaling (Fig. 5g).

We found that 21 GWAS loci were associated with lipid and cholesterol metabolism adDEG genes, which is consistent with broad dysregulation of brain cholesterol homeostasis in AD⁴⁴. For example, *RORA* regulates⁴⁵ pathological retinal angiogenesis by repressing the inflammation repressor *SOCS3*, which is itself also upregulated in cEndo and vEndo cells in AD in our data (Fig. 5b and Extended Data Fig. 10b). *ABCA1* (Fig. 5b and Extended Data Fig. 9c) was linked to four AD-associated intronic variants and upregulated in AD PERs, causing increased PER cholesterol efflux to APOE⁴⁶. *SCARB1* was linked to its own AD-associated intronic variant (rs78194510) (Fig. 5b and Extended Data Fig. 9d), which was highly expressed in cEndo cells and PERs in AD and mediates HDL signaling in endothelial cells^{47,48}.

We also found that nine AD GWAS loci were associated with immune response, insulin secretion and neurodegenerative pathogenesis, including *IL6* and *IL6R* (Fig. 5b and Extended Data Fig. 9e), which were highly expressed in the cEndo cells of individuals with AD, suggesting that the immune response of endothelial cells may be a prominent feature of AD blood vessels^{49,50}. *MYRIP*, which was associated with the 100-kb upstream variant rs9832461, was downregulated in the cEndo cells of individuals with AD (Extended Data Fig. 9f). *PFDNI*, which showed decreased expression in the vSMCs of patients with

AD, was linked to the AD variant rs11168036 (Extended Data Fig. 9g), suggesting dysregulation of the protein-folding machinery in cerebrovascular cells in AD.

Second, we searched for indirect genetic evidence for vascular adDEGs whose upstream regulators were directly linked to AD-associated variants (*trans*-regulation) (Fig. 6a). Five of our previously predicted (Fig. 3a,b) upstream regulators (*YAP1*, *TCF7L2*, *NFIC*, *ETS1*, *DACH1*) were directly linked to AD-associated variants, representing a 2.9-fold enrichment, given that only 33 TFs lie in AD-associated loci (Fisher’s exact test, $P = 0.04$). The first four TFs were also predicted to be upstream regulators of cell type-specific marker genes in our earlier analysis (Fig. 1e). These AD-associated regulators targeted 559 vascular adDEGs across five cell types (Fig. 6a and Supplementary Table 11), showing biologically meaningful enrichment. For example, the targets of *ETS1* were significantly enriched in the cytokine and growth factor stimulus response in cEndo cells, which is consistent with previous work^{51–54}.

Third, we searched for indirect genetic evidence for vascular adDEGs that were coexpressed with ligand–receptor pairs, when those ligands are (1) directly linked to AD-associated variants and (2) adDEGs are located in nonvascular brain cells. We called this third type of regulation intercellular regulation. We used our previously annotated correlated module pairs (degModules) (Fig. 4 and Extended Data Fig. 8) and searched for AD-linked adDEG ligands indicative of potential genetic effects. We found 54 pairs (24 upregulated and 30 downregulated in AD) with ligands proximal to AD-associated genetic loci (Fig. 6b), implicating 611 vascular adDEGs that are linked to 12 AD-associated ligands and 13 receptors (in 18 different ligand–receptor pairs). The 12 AD-associated ligands represent a significant enrichment

over expectation (odds ratio (OR) = 2.52, $P = 0.0016$, Fisher's exact test). Seven of these 12 ligands showed single-cell expression quantitative trait locus (sc-eQTL) linking evidence, three showed tissue-level brain eQTL evidence from Genotype-Tissue Expression (GTEx) and seven showed Hi-C loop linking evidence, including six with multiple lines of evidence (Fig. 6b, column 2). Their downstream genes were enriched in at least 17 different biological functions (Fig. 6c and Supplementary Table 12). For example, we observed that *APOE*, the strongest genetically associated AD gene, showed increased expression in microglia and decreased expression in astrocytes, and interacted with *LRP6* (ref. 55) (downregulated in AD) to regulate the expression of genes in AD PERs that were significantly enriched for cell junction and migration.

Taken together, 1,010 of 2,676 vascular adDEGs in AD can be associated with AD genetics using *cis*, *trans* or intercellular signaling regulatory mechanisms (Extended Data Fig. 9a,h and Supplementary Table 13). This suggests that the effects of genetic risk factors on the cerebrovasculature may contribute to the pathogenesis of AD through intracellular dysfunction and intercellular communication between vascular cell types and neural, glial and microglial cells in the brain parenchyma and immune cells in peripheral blood.

APOE genotype and cognitive decline in vascular cells

To elucidate the molecular mechanisms and vascular cell types potentially mediating the effects of APOE $\epsilon 4$ on BBB dysfunction and cognitive decline, we searched for APOE genotype-associated DEGs (apoeDEGs) between APOE $\epsilon 3$ homozygous individuals (E3, $n = 251$) and carriers of one or two APOE $\epsilon 4$ alleles (E4, $n = 101$ heterozygous $\epsilon 3$ individuals and $n = 7$ homozygous $\epsilon 4$ individuals) (Extended Data Fig. 10a, Supplementary Table 1 and Methods).

We found 2,482 apoeDEGs (Fig. 7a and Supplementary Table 14), which were largely evenly distributed across cell types (120 APOE4 upregulated and 120 APOE4 downregulated on average) and similar in count to the number of adDEGs. While only a median of 4% of APOE differential genes were shared with AD differential genes, the overlap between apoeDEGs and adDEGs was highly significant for a subset of cell types. For cEndo cells, 36% of upregulated apoeDEGs were also upregulated adDEGs (12-fold enrichment, $P = 10^{-32}$, Fisher's exact test) and 21% of downregulated apoeDEGs were also downregulated adDEGs (12-fold, $P = 10^{-20}$). Strong apoeDEG–adDEG agreement was found for FIB1 and PER1 cells (tenfold to 14-fold enrichment), while weaker agreement was found for PER2 and vEndo upregulated genes (sixfold to eightfold).

We searched for enriched biological pathways in upregulated and downregulated apoeDEGs in each cell type (Fig. 7b and Supplementary Table 15). In cEndo cells, downregulated apoeDEGs (E4-down) were significantly enriched in transport across the BBB, cell junction organization and regulation of sprouting angiogenesis. In PERs, downregulated apoeDEGs were enriched in cell migration regulation, transport across the BBB and cell–cell junction maintenance (Fig. 7b), which is consistent with reports of APOE $\epsilon 4$ individuals showing reduced cerebral blood flow⁵⁶ and increased cerebrovascular abnormalities⁵⁷.

We next evaluated the correlation of all apoeDEGs with cognitive decline and found that upregulated apoeDEGs (E4-up) were primarily associated with cognitive decline across all cell types, while downregulated apoeDEGs (E4-down) were primarily associated with cognitive resilience (Fig. 7c and Extended Data Fig. 10b). This effect was strongest for cEndo ($P < 10^{-22}$), vEndo ($P < 10^{-11}$), FIB1 ($P < 10^{-11}$) and PER1 ($P < 10^{-8}$) cells, with substantial and highly significant differences in cognitive decline correlation between E4-up and E4-down genes. Our results are consistent with previous findings that cPERs might mediate the effect of APOE4 on cognitive decline⁵⁸, and indicate that cEndo and FIB1 cells might have equal or even more important roles.

We further identified APOE genotype-conditional, cognitive decline-correlated DEGs (cogDEGs) (Fig. 7d, Supplementary Table 16 and Methods), distinguishing 'decline-up' cogDEGs, which are

positively correlated with cognitive decline, and 'decline-down' cogDEGs, which are negatively correlated with cognitive decline. APOE4 individuals showed more cogDEGs than APOE3 individuals (>1.5-fold) for cEndo, vEndo, PER1 and FIB1 (Fig. 7d), especially for decline-up genes (2.1-fold), suggesting that specific cerebrovascular cell types might mediate the contribution of the APOE $\epsilon 4$ allele to cognitive decline. Comparing APOE3 with APOE4 cogDEGs, we found that the two sets were largely distinct, with only approximately 5% overall of cogDEGs in common between APOE4 and APOE3 (Fig. 7e), suggesting distinct transcriptional changes and specific mechanisms of cognitive decline between $\epsilon 3$ and $\epsilon 4$ carriers.

To further investigate the functions of APOE genotype-conditional cogDEGs, we performed GO enrichment analysis for E3-specific, E4-specific and E3–E4-shared cogDEGs in capillary cell types (cEndo and PER1) (Fig. 7f and Supplementary Table 17). For cEndo decline-up cogDEGs, APOE4-specific enrichment included lipid and cytokine response and apoptotic processes; APOE3 enrichment included vascular transport, negative regulation of cell migration and cell matrix adhesion. For cEndo decline-down cogDEGs, APOE4-specific enrichment included blood vessel development, regulation of BMP signaling and neurotransmitter transport; APOE3 enrichment included positive regulation of endothelial cell migration and extracellular structure organization. For PER1 decline-up cogDEGs, APOE4-specific enrichment included cytokine response, cell–cell junction assembly and apoptosis; APOE3 enrichment included negative regulation of SMC migration and Notch signaling, and autophagy. For PER1 decline-down cogDEGs, APOE4-specific enrichment included BBB-related functions (BBB maintenance, Notch signaling, contraction regulation), whereas APOE3 enrichment included lipid and chemical homeostasis and cell junction assembly, suggesting that APOE $\epsilon 4$ -dependent cognitive decline may be primarily mediated by PER1 PERs (Fig. 7f).

Discussion

In this study, we analyzed the transcriptome of 22,514 single nuclei, identified the molecular signatures and upstream regulators of 11 brain vascular cell types and characterized region-specific and region-expressed genes and pathways. We identified 2,676 AD-associated adDEGs with strong cell type specificity. The identified adDEGs were enriched in multiple biological pathways broadly across cell types and specifically in single-cell types. We experimentally validated the upregulation of *INSR* and *COL4A1* in AD endothelial cells, and the upregulation of *APOD* and downregulation of *SLC6A1* in AD PERs using RNA in situ hybridization and IHC staining. We also predicted upstream regulators of adDEGs and grouped them into collaborative regulator modules, potentially driven by primary regulators. Our analysis provides a general framework for understanding how regulators collaboratively control dysfunctional gene programs in disease and may aid in prioritizing therapeutic targets to restore the function of AD differential genes, developing induced pluripotent stem cell-derived vasculature and planning perturbation experiments.

We next investigated differential cell–cell communication of neurovascular units in AD. Methodologically, we introduced a new computational framework and identified 577 instances of AD differential cell–cell communication and mediated signaling pathways. The dynamics of multicellular interactions in AD call attention to the development of multicellular in vitro systems and provide a specific point of view at a multicellular level for therapy in the future.

Moreover, our study yielded insights on interpreting AD genetic variants from genome-wide human genetic studies in cerebrovascular cell types. We proposed and studied three types of mechanisms to understand how AD variants are associated with vascular differential genes in AD: (1) direct regulation in a *cis* way; (2) indirect regulation in a *trans* way through regulators; and (3) indirect regulation through intercellular signaling pathways. Altogether, we observed that 1,010 (37.7%) adDEGs could be associated with the genetics of AD, suggesting

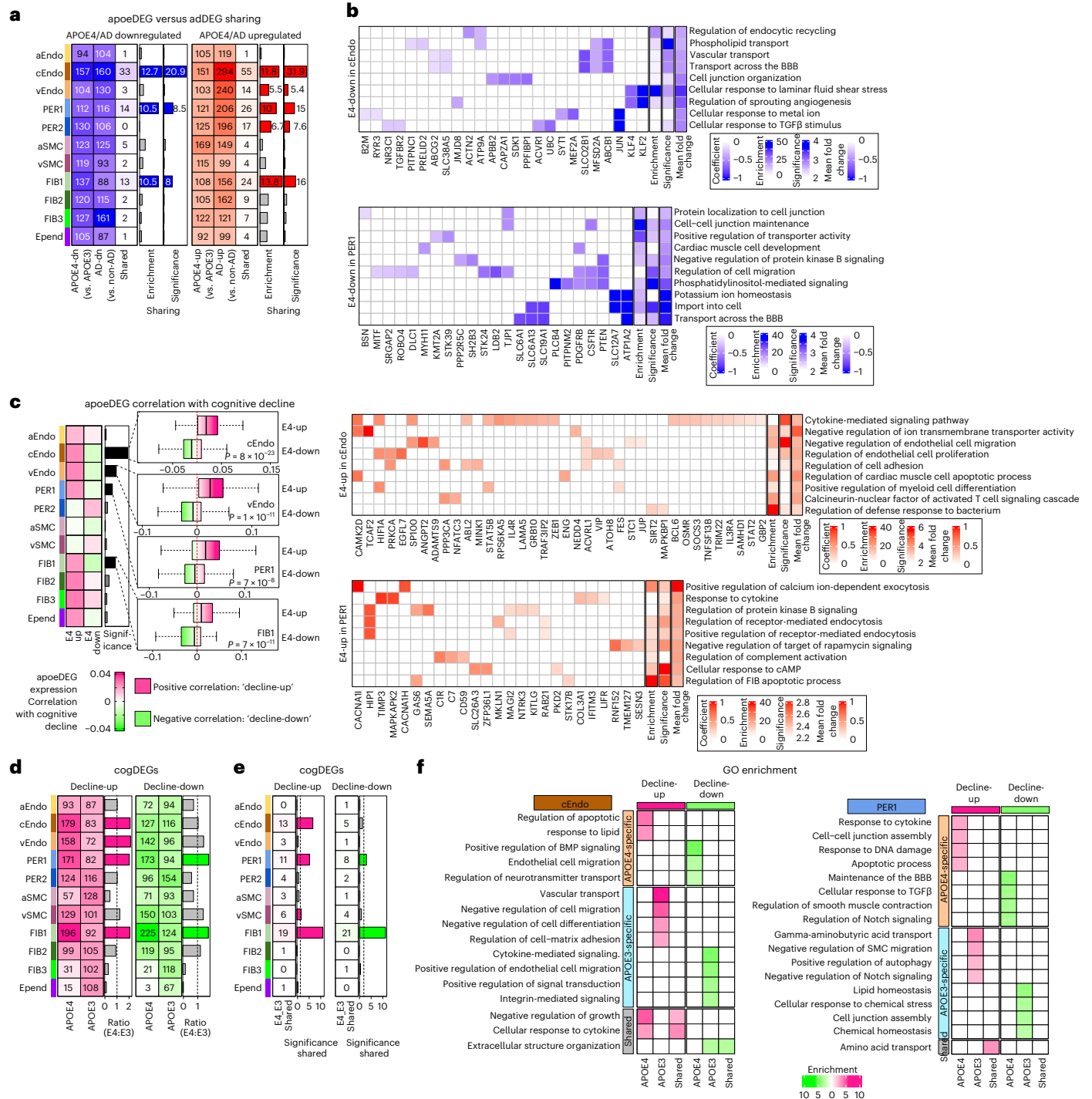


Fig. 7 | APOE4-associated transcriptional changes and cognitive decline.

a, Comparison of apoeDEGs and adDEGs for each cell type. The heatmaps show the number of upregulated and downregulated apoeDEGs, adDEGs and overlapping DEGs in the APOE4 or AD group. The fold enrichment and adjusted *P* (two-sided Fisher’s exact test, *P* < 0.05 as the cutoff) are shown in the bar plot. **b**, Enriched GO biological processes in apoeDEGs in cEndo and PER1 cells. Enrichr was used (proportion test, adjusted *P* < 0.05 as the cutoff). The color of the heatmap for each term–gene pair represents the effect size. The last three columns show enrichment, the significance of each term and the average effect size of the genes. Representative terms are shown in bold. **c**, Difference of correlation of apoeDEGs with cognitive decline between upregulated and downregulated apoeDEGs in the APOE4 group. The correlation between apoeDEGs and cognitive decline was calculated. The heatmap shows the average correlation. The bar plot shows the significance of a higher correlation of apoeDEGs with cognitive decline. The box plot (right) shows the distribution of

the correlation with cognitive decline in E4 upregulated and E4 downregulated genes (*n* = 428 individuals). The box starts in the first quantile (25%) and ends in the third (75%). The line inside the box plot represents the median. The two whiskers without outliers represent the maximum and minimum. A *t*-test was used (adjusted *P* < 0.05 as the cutoff). The *P* value is shown. **d**, Number of decline upregulated (left) and decline downregulated (right) genes in APOE4 and APOE3 individuals. The bar plot shows the ratio of cogDEGs in E4 versus E3 in several cell types with a ratio greater than 1.5-fold as the cutoff. **e**, Number and significance of overlapping decline upregulated and downregulated genes between APOE4 and APOE3 individuals. The bar plot shows the significance of the overlap (two-sided Fisher’s exact test, adjusted *P* < 0.05). **f**, Enriched biological functions of APOE genotype-specific shared decline upregulated and downregulated genes in cEndo cells and PERs. Enrichr was used (proportion test, adjusted *P* < 0.05). The enrichment scores are shown in the heatmap.

the importance of understanding BBB dysregulation in AD from a genetic perspective and providing a paradigm of associating disease risk genes with DEGs that can be widely applied in multiple scenarios.

Finally, our study sheds light on the molecular and cellular bases of the association between cerebrovasculature and APOE4-associated cognitive decline, suggesting the potential for therapeutic targets related to BBB dysfunction in specific APOE genotypes. Given the limited number of vascular cells, especially for rare cell types in APOE4, further targeted studies are needed to comprehensively understand the association and causality among APOE genotype, BBB function, cognitive decline and AD. The computational predictions of apoeDEGs in this study, as well as adDEGs, regulators, signaling pathways, cell–cell interactions and AD risk genes in vascular cell types, are expected to be experimentally and independently confirmed in future work.

Overall, our multiregion molecular atlas of differential human cerebrovasculature genes and pathways in AD provides an important foundation for guiding AD therapeutics, especially for early-stage interventions where the BBB is increasingly being recognized as having a central role.

Online content

Any methods, additional references, Nature Portfolio reporting summaries, source data, extended data, supplementary information, acknowledgements, peer review information; details of author contributions and competing interests; and statements of data and code availability are available at <https://doi.org/10.1038/s41593-023-01334-3>.

References

- Sweeney, M. D., Kisler, K., Montagne, A., Toga, A. W. & Zlokovic, B. V. The role of brain vasculature in neurodegenerative disorders. *Nat. Neurosci.* **21**, 1318–1331 (2018).
- Sweeney, M. D., Sagare, A. P. & Zlokovic, B. V. Blood–brain barrier breakdown in Alzheimer disease and other neurodegenerative disorders. *Nat. Rev. Neurol.* **14**, 133–150 (2018).
- Vanlandewijck, M. et al. A molecular atlas of cell types and zonation in the brain vasculature. *Nature* **554**, 475–480 (2018).
- Garcia, F. J. et al. Single-cell dissection of the human brain vasculature. *Nature* **603**, 893–899 (2022).
- Yang, A. C. et al. A human brain vascular atlas reveals diverse mediators of Alzheimer's risk. *Nature* **603**, 885–892 (2022).
- Wilhelm, I., Nyúl-Tóth, Á., Suciú, M., Hermenean, A. & Krizbai, I. A. Heterogeneity of the blood–brain barrier. *Tissue Barriers* **4**, e1143544 (2016).
- Tran, K. A. et al. Endothelial β -catenin signaling is required for maintaining adult blood–brain barrier integrity and central nervous system homeostasis. *Circulation* **133**, 177–186 (2016).
- Slater, S. C. et al. MicroRNA-532-5p regulates pericyte function by targeting the transcription regulator BACH1 and Angiotensin-1. *Mol. Ther.* **26**, 2823–2837 (2018).
- Zhang, X. et al. High-resolution mapping of brain vasculature and its impairment in the hippocampus of Alzheimer's disease mice. *Nat'l Sci. Rev.* **6**, 1223–1238 (2019).
- Lau, S.-F., Cao, H., Fu, A. K. Y. & Ip, N. Y. Single-nucleus transcriptome analysis reveals dysregulation of angiogenic endothelial cells and neuroprotective glia in Alzheimer's disease. *Proc. Natl Acad. Sci. USA* **117**, 25800–25809 (2020).
- Velmeshev, D. et al. Single-cell genomics identifies cell type-specific molecular changes in autism. *Science* **364**, 685–689 (2019).
- Ruzicka, W. B. et al. Single-cell dissection of schizophrenia reveals neurodevelopmental-synaptic axis and transcriptional resilience. Preprint at *medRxiv* <https://doi.org/10.1101/2020.11.06.20225342> (2020).
- Montagne, A. et al. Blood–brain barrier breakdown in the aging human hippocampus. *Neuron* **85**, 296–302 (2015).
- Elali, A. & Rivest, S. The role of ABCB1 and ABCA1 in beta-amyloid clearance at the neurovascular unit in Alzheimer's disease. *Front. Physiol.* **4**, 45 (2013).
- van Assema, D. M. E. et al. Blood–brain barrier P-glycoprotein function in Alzheimer's disease. *Brain* **135**, 181–189 (2012).
- Hamilton, N. B., Attwell, D. & Hall, C. N. Pericyte-mediated regulation of capillary diameter: a component of neurovascular coupling in health and disease. *Front. Neuroenergetics* **2**, 5 (2010).
- Nortley, R. et al. Amyloid β oligomers constrict human capillaries in Alzheimer's disease via signaling to pericytes. *Science* **365**, eaav9518 (2019).
- Wang, F. et al. RNAscope: a novel in situ RNA analysis platform for formalin-fixed, paraffin-embedded tissues. *J. Mol. Diagn.* **14**, 22–29 (2012).
- Bhatia, S., Kim, W. S., Shepherd, C. E. & Halliday, G. M. Apolipoprotein D upregulation in Alzheimer's disease but not frontotemporal dementia. *J. Mol. Neurosci.* **67**, 125–132 (2019).
- Leng, K. et al. Molecular characterization of selectively vulnerable neurons in Alzheimer's disease. *Nat. Neurosci.* **24**, 276–287 (2021).
- Szklarczyk, D. et al. The STRING database in 2021: customizable protein–protein networks, and functional characterization of user-uploaded gene/measurement sets. *Nucleic Acids Res.* **49**, D605–D612 (2021).
- Kim, K.-J. et al. STAT3 activation in endothelial cells is important for tumor metastasis via increased cell adhesion molecule expression. *Oncogene* **36**, 5445–5459 (2017).
- Wei, D. et al. Stat3 activation regulates the expression of vascular endothelial growth factor and human pancreatic cancer angiogenesis and metastasis. *Oncogene* **22**, 319–329 (2003).
- Zhang, B. et al. A dynamic H3K27ac signature identifies VEGFA-stimulated endothelial enhancers and requires EP300 activity. *Genome Res.* **23**, 917–927 (2013).
- Marconcini, L. et al. c-fos-induced growth factor/vascular endothelial growth factor D induces angiogenesis in vivo and in vitro. *Proc. Natl Acad. Sci. USA* **96**, 9671–9676 (1999).
- Battle, T. E., Lynch, R. A. & Frank, D. A. Signal transducer and activator of transcription 1 activation in endothelial cells is a negative regulator of angiogenesis. *Cancer Res.* **66**, 3649–3657 (2006).
- Paneni, F. et al. Deletion of the activated protein-1 transcription factor JunD induces oxidative stress and accelerates age-related endothelial dysfunction. *Circulation* **127**, 1229–1240 (2013).
- Wang, N. et al. c-Jun triggers apoptosis in human vascular endothelial cells. *Circ. Res.* **85**, 387–393 (1999).
- Mahamud, M. R. et al. GATA2 controls lymphatic endothelial cell junctional integrity and lymphovenous valve morphogenesis through *miR-126*. *Development* **146**, dev184218 (2019).
- Chen, M. B. et al. Brain endothelial cells are exquisite sensors of age-related circulatory cues. *Cell Rep.* **30**, 4418–4432 (2020).
- Zhao, L. et al. Pharmacologically reversible zonation-dependent endothelial cell transcriptomic changes with neurodegenerative disease associations in the aged brain. *Nat. Commun.* **11**, 4413 (2020).
- Ohnesorge, N. et al. Erk5 activation elicits a vasoprotective endothelial phenotype via induction of Kruppel-like factor 4 (KLF4). *J. Biol. Chem.* **285**, 26199–26210 (2010).
- Pugacheva, E. M. et al. CTCF mediates chromatin looping via N-terminal domain-dependent cohesin retention. *Proc. Natl Acad. Sci. USA* **117**, 2020–2031 (2020).
- Xu, L., Nirwane, A. & Yao, Y. Basement membrane and blood–brain barrier. *Stroke Vasc. Neurol.* **4**, 78–82 (2019).
- McMillin, M. A. et al. TGF β 1 exacerbates blood–brain barrier permeability in a mouse model of hepatic encephalopathy via upregulation of MMP9 and downregulation of claudin-5. *Lab. Invest.* **95**, 903–913 (2015).

36. Rustenhoven, J. et al. TGF- β 1 regulates human brain pericyte inflammatory processes involved in neurovasculature function. *J. Neuroinflammation* **13**, 37 (2016).
37. Kashima, R. & Hata, A. The role of TGF- β superfamily signaling in neurological disorders. *Acta Biochim. Biophys. Sin.* **50**, 106–120 (2018).
38. van Crujisen, H., Giaccone, G. & Hoekman, K. Epidermal growth factor receptor and angiogenesis: opportunities for combined anticancer strategies. *Int. J. Cancer* **117**, 883–888 (2005).
39. Jansen, I. E. et al. Genome-wide meta-analysis identifies new loci and functional pathways influencing Alzheimer's disease risk. *Nat. Genet.* **51**, 404–413 (2019).
40. Kunkle, B. W. et al. Genetic meta-analysis of diagnosed Alzheimer's disease identifies new risk loci and implicates A β , tau, immunity and lipid processing. *Nat. Genet.* **51**, 414–430 (2019).
41. Kang, S. et al. Potential novel genes for late-onset Alzheimer's disease in East-Asian descent identified by APOE-stratified genome-wide association study. *J. Alzheimers Dis.* **82**, 1451–1460 (2021).
42. Pallejà, A., Horn, H., Eliasson, S. & Jensen, L. J. DistILD database: diseases and traits in linkage disequilibrium blocks. *Nucleic Acids Res.* **40**, D1036–D1040 (2012).
43. Buniello, A. et al. The NHGRI-EBI GWAS Catalog of published genome-wide association studies, targeted arrays and summary statistics 2019. *Nucleic Acids Res.* **47**, D1005–D1012 (2019).
44. Chang, T.-Y., Yamauchi, Y., Hasan, M. T. & Chang, C. Cellular cholesterol homeostasis and Alzheimer's disease. *J. Lipid Res.* **58**, 2239–2254 (2017).
45. Sun, Y. et al. Nuclear receptor ROR α regulates pathologic retinal angiogenesis by modulating SOCS3-dependent inflammation. *Proc. Natl Acad. Sci. USA* **112**, 10401–10406 (2015).
46. Saint-Pol, J. et al. Brain pericytes ABCA1 expression mediates cholesterol efflux but not cellular amyloid- β peptide accumulation. *J. Alzheimers Dis.* **30**, 489–503 (2012).
47. Robert, J., Osto, E. & von Eckardstein, A. The endothelium is both a target and a barrier of HDL's protective functions. *Cells* **10**, 1041 (2021).
48. Husemann, J. & Silverstein, S. C. Expression of scavenger receptor class B, type I, by astrocytes and vascular smooth muscle cells in normal adult mouse and human brain and in Alzheimer's disease brain. *Am. J. Pathol.* **158**, 825–832 (2001).
49. Rothaug, M., Becker-Pauly, C. & Rose-John, S. The role of interleukin-6 signaling in nervous tissue. *Biochim. Biophys. Acta* **1863**, 1218–1227 (2016).
50. Choi, J. M., Rotimi, O. O., O'Carroll, S. J. & Nicholson, L. F. B. IL-6 stimulates a concentration-dependent increase in MCP-1 in immortalised human brain endothelial cells. *F1000Res.* **5**, 270 (2016).
51. Wei, G. et al. Ets1 and Ets2 are required for endothelial cell survival during embryonic angiogenesis. *Blood* **114**, 1123–1130 (2009).
52. Park, R. et al. Yap is required for ependymal integrity and is suppressed in LPA-induced hydrocephalus. *Nat. Commun.* **7**, 10329 (2016).
53. Xie, C. et al. Yap1 protein regulates vascular smooth muscle cell phenotypic switch by interaction with myocardin. *J. Biol. Chem.* **287**, 14598–14605 (2012).
54. Shen, T. et al. YAP1 plays a key role of the conversion of normal fibroblasts into cancer-associated fibroblasts that contribute to prostate cancer progression. *J. Exp. Clin. Cancer Res.* **39**, 36 (2020).
55. Go, G.-W. & Mani, A. Low-density lipoprotein receptor (LDLR) family orchestrates cholesterol homeostasis. *Yale J. Biol. Med.* **85**, 19–28 (2012).
56. Thambisetty, M., Beason-Held, L., An, Y., Kraut, M. A. & Resnick, S. M. APOE ϵ 4 genotype and longitudinal changes in cerebral blood flow in normal aging. *Arch. Neurol.* **67**, 93–98 (2010).
57. Leaston, J. et al. Neurovascular imaging with QUTE-CE MRI in APOE4 rats reveals early vascular abnormalities. *PLoS ONE* **16**, e0256749 (2021).
58. Montagne, A. et al. APOE4 leads to blood–brain barrier dysfunction predicting cognitive decline. *Nature* **581**, 71–76 (2020).

Publisher's note Springer Nature remains neutral with regard to jurisdictional claims in published maps and institutional affiliations.

Springer Nature or its licensor (e.g. a society or other partner) holds exclusive rights to this article under a publishing agreement with the author(s) or other rightsholder(s); author self-archiving of the accepted manuscript version of this article is solely governed by the terms of such publishing agreement and applicable law.

© The Author(s), under exclusive licence to Springer Nature America, Inc. 2023, corrected publication 2023

Methods

Human brain samples from ROSMAP

The human brain tissues used in this study were obtained from the Religious Orders Study and Rush Memory and Aging Project (ROSMAP), each approved by the institutional review board of Rush University Medical Center, with informed consent, an Anatomic Gift Act for organ donation and a repository consent to allow the data to be shared⁵⁹. Quantitative clinical and pathological phenotypes of AD were used to assess disease severity. These included global cognition proximate to death and a measure of global AD pathology, as well as the molecularly specific amyloid- β and PHF-tau tangles. Specifically, we performed *k*-mean clustering on this quantitative matrix after *z*-score normalization to group all patients in the cohort into *k* = 3 clusters: non-AD (controls); early AD; and late AD (Supplementary Fig. 1a). Controls were defined as individuals with little to no AD pathology, whereas cases (early and late AD) included a spectrum of AD and cognition pathology. Thus, case status was based on both AD and cognition pathology; other variables were allowed to freely associate^{60–64}. In this study, we then combined individuals with early and late AD as one AD group given the limited number of vascular cells. We profiled the PFC for 409 individuals and four other regions for a subset of 48 individuals, including mid-temporal cortex, angular gyrus, entorhinal cortex, thalamus and hippocampus for a subset of 65 individuals and an additional 19 individuals (Supplementary Table 1). We had 455 samples in the PFC including 364 individuals with 1 sample, 44 individuals with 2 samples and 1 individual with 3 samples. For other regions, there was one sample per individual (47 in the angular gyrus, mid-temporal cortex and thalamus; 45 in the entorhinal cortex; 84 in hippocampus). Thus, we had a total of 725 samples from 428 individuals.

Isolation of nuclei from frozen postmortem brain tissue and snRNA-seq

We isolated nuclei from frozen postmortem brain tissue as described previously (Mathys et al.⁶⁵) with some modifications. Briefly, we homogenized the brain tissue in 700 μ l homogenization buffer and filtered the homogenate through a 40- μ m cell strainer (Corning), added 450 μ l working solution and loaded it as a 25% OptiPrep solution on top of a 30%/40% OptiPrep density gradient (750 μ l 30% OptiPrep solution, 300 μ l 40% OptiPrep solution). We separated the nuclei by centrifugation using a fixed rotor, tabletop centrifuge (for 5 min at 10,000g and 4 °C). We collected the nuclear pellet at the 30%/40% interphase, transferred it to a new tube, washed it twice with 1 ml ice-cold PBS containing 0.04% BSA (centrifuged for 3 min at 300g and 4 °C) and finally resuspended it in 100 μ l PBS containing 0.04% BSA. After counting, we diluted the nuclei to a concentration of 1,000 nuclei per μ l. We used the isolated nuclei for the droplet-based 10 \times scRNA-seq assay, targeting 5,000 nuclei per brain region and individual, and prepared libraries using the Chromium Single-Cell 3' Reagent Kits v3 (10X Genomics) according to the manufacturer's protocol. We sequenced the pooled libraries using the NovaSeq 6000 S2 sequencing Kit (100 cycles, Illumina).

snRNA-seq data preprocessing

We aligned the raw reads to the human reference genome version GRCh38 (pre-mRNA) and quantified the gene counts using Cell Ranger v3.0.1 (10X Genomics)⁶⁶. The generated cell-gene count matrix was processed with the Seurat v.4.0.3 (ref. 67). We used a threshold of 500 unique molecular identifiers to select cells and a cutoff value of 50 cells to select genes for further analysis. We filtered out the cells with more than 10% mitochondrial genes. The gene count was normalized by the total counts for each cell, multiplied by 10,000, and then log-transformed. We identified the top 2,000 highly variable genes for dimension reduction using the Seurat default parameters. We used the top 30 principal components (PCs) as input to calculate the first

two components of UMAP. We used Harmony for batch correction⁶⁸ and DoubletFinder to estimate the doublet score with a 7.5% doublet formation rate⁶⁹. Cells with high doublet scores (0.2 as the cutoff) were discarded for further analysis. We used a 0.5 resolution to identify clusters. After generating clusters, clusters showing high expression of markers of two or more cell types were also treated as doublets and removed from further analysis.

In silico sorting to enrich vascular cells and cell type annotation

For the full datasets with all cell types (2.8 million cells), we first annotated the cell type for each cluster based on the canonical markers of major cell types in the brain (including excitatory and inhibitory neurons, astrocytes, oligodendrocytes, oligodendrocyte progenitor cells (OPCs), microglia and vascular cells)⁶⁵ and the enrichment of a large set of markers⁷⁰ in highly expressed genes of each cluster. We next calculated the cell type scores (that is, astrocyte, oligodendrocyte, microglia) for each cell, which were represented by the average expression of a group of markers for each cell type⁷⁰. Cells were then selected as vascular cells for further integrative analysis only if (1) the clusters cells belong to were annotated as vascular cell types and (2) cells had the highest score for vascular cell types and (3) the score for vascular cell types was twofold higher than the second highest score. For all vascular cells, we followed the same pipeline to perform dimensional reduction and clustering with the same parameter as full datasets. We had previously reported data from control individuals⁴; in this study, we report data from individuals with AD.

Comparison with public datasets

We downloaded the processed dataset from Yang et al.⁵, who performed a vessel enrichment protocol to enrich brain vascular cells in samples of brain tissue from individuals with AD and controls (GSE163577)^{5,10}. We integrated our data with the vessel enrichment-based dataset reported in Yang et al.⁵ by identifying cross-dataset pairs of cells that in a matched biological state ('anchors') to correct for technical differences between datasets. The combination of highly variable genes (top 2,000 for each dataset) were used for principal component analysis (PCA). The top 30 PCs were used for nonlinear dimensionality reduction (UMAP). We visualized the data using UMAP with cell type labels from the original study. We also tested the enrichment of cell type marker genes between the two studies using a Fisher's exact test with multiple testing (with all expressed genes as the background) to evaluate if the cell types uncovered by the two studies were consistent (FDR < 0.05 as the cutoff).

We also downloaded the processed dataset from Lau et al. (GSE157827)¹⁰, who performed snRNA-seq to capture all cell types in the brain without any enrichment, for comparison with the present study. Lau et al. did not annotate the detailed vascular cell types but instead used 'endothelial' as the annotation for the vascular cells in their data. We performed clustering to further annotate the specific vascular cell types including endothelial cells, PERs, SMCs and FIBs. Given the limited number of rare cell populations, we only identified DEGs between individuals with AD and controls in endothelial cells with enough power.

Identification of DEGs between cell types and between brain regions

We used a Wilcoxon rank-sum test in Seurat with customized parameters (min.pct = 0.25, logfc.threshold = 0.25) to identify (1) highly expressed genes for each cell type or subtype compared with the cells and (2) DEGs between brain regions for each cell subtype that had more than 50 cells in each region. We considered a gene differentially expressed if it was detected in at least 25% of cells and the log fold change was higher than 0.25.

Identification of DEGs between individuals with AD and controls

To compare individuals with AD and controls, we applied MAST (Model-based Analysis of Single-cell Transcriptomics), a single-cell-based method, to measure the statistical significance for each gene based on a linear model⁷¹. The covariates, including the number of cells, the number of expressed genes, age, sex, PMI, ethnic group, batch, brain region and other dementia-related pathology (Lewy body dementia, Parkinson's disease and vascular contributions to cognitive impairment and dementia (VCID)) were controlled in the model. The genes with $P < 0.01$ and coefficient greater than 0.02 were selected as adDEGs for further analysis. To confirm that these differences are biological and not statistical artifacts, we permuted the annotation of AD status for each individual 1,000 times and identified the adDEGs using the same computational pipeline, and found that the number of adDEGs was significantly higher than expected by chance ($P < 0.05$).

We also applied a pseudobulk-based method, edgeR⁷², to detect the DEGs for each cell type between individuals with AD and controls using the same covariates as above ($P < 0.01$). We then tested if, for the same cell type, the adDEGs identified by the two methods (MAST and edgeR) significantly overlapped using Fisher's exact test with all expressed genes as background and adjusted $P < 0.01$. We found that adDEGs were highly consistent between the two methods.

Finally, we also performed a downsampling analysis to confirm the consistency of the number of adDEGs in the cEndo cell subtype using different numbers of cells (1,000, 2,000, 3,000, 4,000, 5,000 and the original 6,195). Specifically, we randomly selected a number of cells without replacement and identified the adDEGs using MAST with the same parameters outlined above. We compared the adDEGs in terms of effect size by evaluating the two parameters. First, we calculated the Pearson's correlation coefficient between each pair of comparisons (that is, between the adDEGs identified in the group of 1,000 cells and in the group of 2,000 cells). Second, we calculated the score defined by the ratio of the number of genes with consistent directional regulation (that is, upregulated in both datasets or downregulated in both datasets) to the number of genes with inconsistent directional regulation. These data are visualized in Extended Data Fig. 4c.

RNA in situ hybridization

For the human postmortem samples, fresh-frozen human PFC samples (area BA9) were embedded in Tissue-Tek O.C.T. Compound (catalog no. 25608-930, Sakura), cut at 10 μm using a cryostat (catalog no. CM3050S, Leica Microsystems) and collected on SuperFrost Plus Slides (catalog no. 12-550-15, Thermo Fisher Scientific). We collected eight sections (one per individual, $n = 4$ controls and $n = 4$ individuals with AD) per slide. Mounted tissue sections were stored at -80°C until further processing. RNAscope Chromogenic 2.5 was used for C1 probe hybridization; xylene was not used before mounting. Probes used in this study included *CD31* (red, catalog no. 548451-C2, Advanced Cell Diagnostic); *INSR* (HD Duplex Reagent Kit, catalog no. 322430, Advanced Cell Diagnostic) was used to perform RNA in situ hybridization according to the manufacturer's instructions with the following modifications: tissue was fixed in 4% paraformaldehyde (PFA) for 30 min; 30 minutes were allowed for C2 probe hybridization overnight at room temperature (green, catalog no. 406411, Advanced Cell Diagnostic), GRM8 (catalog no. 563351, Advanced Cell Diagnostic), APOD (catalog no. 445171, Advanced Cell Diagnostic), ABCC9 (catalog no. 521881, Advanced Cell Diagnostic) and SLC6A1 (catalog no. 545121-C2, Advanced Cell Diagnostic). Images were acquired using the brightfield settings of a ZEISS LSM 900 microscope. We only captured images where the tissue was in focus on the z-plane and did not have any technical artifacts.

RNA in situ hybridization analysis

Images were imported into QuPath (v.0.2.0-m8)⁷³. Vessel segments were identified based on the expression of *CD31*⁺ punctae, which formed

visually distinct vessel-like segments. For example, to define colocalization between endothelial (*CD31*⁺) cells and the *INSR* transcript, we used QuPath⁷³ to annotate cells positive for the red signal (that is, expressing *CD31* transcripts), and then quantified the number of blue punctae (that is, *INSR* transcripts) in each cell. This corresponded to the number of *INSR* transcripts per *CD31*⁺ vessel segment. For each image, we then quantified the number of vessel segments with the number of blue punctae per segment. To account for group differences in overall vascular architecture or *CD31* expression, we normalized the number of punctae per area by calculating the vessel segment area using the Annotations feature in QuPath. To detect individual cells, we used the Analyze function in QuPath. We then determined the frequency distribution for each density quantification between patients with AD and controls.

IHC

Individual PFC specimens were removed from -80°C , covered in O.C.T. (Tissue-Tek) in a cryomold and allowed to set for at least 2 h at -80°C . Tissue blocks were then cut on a cryostat into 20- μm sections and mounted onto a SuperFrost slide. Tissue sections were fixed using 4% PFA (Electron Microscopy Services) in PBS for 1 h, then incubated in the blocking buffer (5% normal donkey serum, 0.5% Triton X-100 in PBS) for 24 h at 4°C . We then used TrueBlack Lipofuscin Autofluorescence Quencher (Biotium) to remove background fluorescence according to the manufacturer's protocol (protocol 1, pretreatment with True-Black). Tissue sections were incubated with primary antibodies for 3 d at 4°C and then washed with PBS three times, followed by incubation with secondary antibodies for 4 h; they were finally mounted with Fluoromount-G Mounting Medium. Sections were imaged using a ZEISS LSM 900 confocal microscope at 20 \times or 63 \times magnification. Images were quantified in Fiji, QuPath and Imaris by an investigator blinded to diagnosis. For primary antibodies, we used Anti-Collagen Type IV Antibody (1:125 concentration, catalog no. AB769, Sigma-Aldrich) and Lectin-488 (1:125 concentration, catalog no. DL-1174, Vector Laboratories).

Prediction of upstream regulators of cell type marker genes

We predicted the upstream regulators of cell type markers using Enrichr in R based on three libraries including TRANSFAC and JASPAR, ChEA and ENCODE TF ChIP-seq data⁷⁴⁻⁷⁶. We used adjusted $P < 0.05$ as a cutoff to select the significant regulators (proportion test in the Enrichr package). We kept the regulators with detected expression in the relevant cell types for further analysis.

Prediction of upstream regulators of adDEGs

We predicted the upstream regulators of adDEGs using Enrichr in R based on three libraries including TRANSFAC and JASPAR, ChEA and ENCODE TF ChIP-seq data⁷⁴⁻⁷⁶. We used adjusted $P < 0.05$ as the cutoff to select the significant regulators. We kept the regulators with detected expression in the relevant cell types for further analysis. We also checked if the regulators were significantly highly expressed in the corresponding cell types, which are highlighted in Fig. 3a,b. We tested the significance of shared targets between each pair of regulators in each gene set and grouped these regulators into coregulatory modules (defined as tfModules) based on the hierarchical clustering of significance ($-\log_{10}(P)$) by Fisher's exact test) using the Euclidean distance of the significance matrix as the input for the function hclust in R with default parameters.

We evaluated the regulators within one tfModule by searching the protein-protein interaction network database STRING²¹ for physical interactions validated by experiments and downloaded the generated network as supporting information in this study. To evaluate if the physical interactions between regulators within the same module were not by chance, we performed a permutation test by randomly selecting the same number of regulators in the databases of regulator targets and

calculating the interaction score defined by the ratio of the number of interactions to the total number of pairs. We permuted 1,000 times to calculate the P value and did multiple testing by FDR adjustment with a cutoff of less than 0.05.

We then generated a matrix of zero-one to represent the regulatory relationships between tfModules and target genes and performed hierarchical clustering to separate target genes into distinct clusters. We calculated the percentage of ones in the block formed by a target gene cluster and regulator module to determine if the target gene cluster was regulated by a tfModule. We used 32% as the cutoff based on the boundary of the bimodal distribution shown in Supplementary Fig. 3. One target gene cluster could be regulated by zero, one or multiple regulator modules, and vice versa.

GO enrichment analysis

We used Enrichr in R to perform enrichment analysis for a GO biological process (proportion test, one-sided, adjusted $P < 0.05$ as the cutoff)^{77,78}. The selected terms were manually combined according to general functions, including immune response, cell proliferation and cell migration.

Prediction of dynamic cell–cell communication in AD

For each cell type (including vascular and nonvascular cell types in our brain datasets), we first clustered adDEGs into coexpression gene modules (defined as degModules) across all individuals (pairwise Pearson correlation coefficient, adjusted $P < 0.05$ as the cutoff) and averaged single-cell expression for each cell type within each individual using the AverageExpression function in Seurat. Then, for each pair of cell types, we generated the Pearson correlation coefficient matrix across all module pairs and estimated the significance using the cor.test function in R. We used an adjusted $P < 0.05$ as the cutoff to select the significantly correlated modules between two cell types. For each gene module, we performed GO enrichment analysis to measure the importance of the module at the pathway level and removed gene modules without enriched biological processes and signaling pathways. We combined four ligand–receptor databases (CellChat⁷⁹, CellPhoneDB⁸⁰, CellTalkDB⁸¹ and SingleCellSignalR⁸²) to annotate the correlated modules as evidence for interacting cell–cell pairs mediated by ligand–receptor signaling pathways. We manually curated the selected ligand–receptor pairs in this study to remove mislabeled or intracellular protein–protein interactions through literature searching and filtering. The final results include the interacting cell types, ligands, ligand-involved functions, receptors, receptor-involved functions, potential targets in signal receiver cell type and directions of cell–cell communication in AD. For each pathway shown in Fig. 4c,d, we tested if it was overrepresented in AD-increased or AD-decreased interactions using a two-sided Fisher's exact test with the complete database as background and $P < 0.01$ as the cutoff.

eQTL analysis in vascular cell types

We first estimated the average expression of each gene in each vascular cell type using a gamma Poisson model with a cell-level sequencing depth parameter and an individual-level mean parameter for each gene within each individual. The mean parameter was estimated by an integrative variational inference algorithm⁸³. We then estimated the confounding factors on the individual-level gene expression matrix in an adaptive way. For each gene, we defined control genes by taking the topmost correlated genes located in different chromosomes. We performed PCA and used the top 50 PCs as covariates.

We next built knock-off filters⁸⁴ for a genotype dosage matrix (0, 1, 2 effect allele counts) sampled from a *cis*-window (1 Mb around the gene body) for each gene. We estimated the PCs of the sampled genotype matrix by conducting singular value decomposition. Using the first factors that account for more than 80% of total genetic variation, we estimated structured confounding factors that capture the

dependency structures across individuals and genetic variants. We estimated the knock-off design matrix using scalable approaches^{85–87}.

We then performed multivariate analysis for each gene by regressing the pseudobulk profiles on the observed and knock-off genotype matrix, respectively. We performed a Bayesian spike-and-slab regression before measuring the posterior inclusion probability (PIP) of each variant. The difference between PIP values on the observed variable and the knock-off counterpart were used to construct knock-off statistics. We determined the threshold for a desired FDR level using the R knockoff package⁸⁸.

Association of adDEGs with the genetics of AD

We downloaded AD GWAS-associated genes based on GWAS catalog annotation⁴³ and the summary statistics from Jansen et al.³⁹, using a subthreshold of $-\log_{10}(P) > 5$ to match the genes from the GWAS catalog annotation. The adDEGs in the AD GWAS catalog were then mapped to AD variants based on the annotation in the catalog. The variant with the lowest P value for each gene was used to label the position in the Manhattan plot. We used four types of linking evidence to evaluate the association between AD variant and candidate genes: (1) physical chromatin conformation capture (Hi-C) looping^{89–92}; (2) correlation-based enhancer–gene links⁹³; (3) brain-, heart- and muscle-specific eQTLs at tissue-level resolution⁹⁴; and (4) vasculature cell type-specific sc-eQTLs (in preparation). AD variant and candidate gene associations with at least two pieces of linking evidence were selected for visualization. The distance between AD variant and gene TSS and its ranking according to that distance among variant-associated genes were also calculated and visualized.

We also evaluated the association between AD variants and predicted regulators of adDEGs using the four types of linking evidence mentioned above. We calculated the number of AD variant targets for each AD-associated regulator for each cell type and plotted the heatmap to show if the regulation is cell type-specific or cell type-shared. Similarly, we evaluated the associations between AD variant and ligand that mediate AD-related cell–cell communication using the four types of linking evidence, and performed functional enrichment analysis for each target set to measure the functions of those adDEGs as the downstream targets of AD-associated ligands in vascular cell types.

Identification of DEGs between APOE3 and APOE4 individuals

To compare DEGs between APOE3 and APOE4 individuals, we applied MAST to measure the statistical significance for each gene based on a linear model⁷¹. The covariates, including the number of cells, the number of expressed genes, age, sex, PMI, ethnic group, batch, brain region, and AD status and other dementia-related pathology (Lewy body dementia, Parkinson's disease and VCID), were controlled in the model. Genes with a $P < 0.01$ and a coefficient greater than 0.02 were selected for further analysis.

Identification of APOE genotype-conditional cognitive decline-associated genes

To identify APOE genotype-conditional, cognitive decline-associated genes, we first defined APOE $\epsilon 3$ homozygous individuals and APOE $\epsilon 4$ carriers as APOE3 and APOE4 groups, respectively. For each group, we applied MAST to measure the statistical significance of correlation with cognitive decline for each gene based on a linear model⁷¹. Covariates, including the number of cells, the number of expressed genes, age, sex, PMI, ethnic group, batch, brain region, and AD status and other dementia-related pathology (Lewy body dementia, Parkinson's disease and VCID) were controlled in the model. Genes with a $P < 0.01$ and a coefficient greater than 0.02 were selected for further analysis.

Reporting summary

Further information on research design is available in the Nature Portfolio Reporting Summary linked to this article.

Data availability

Count matrices and metadata for all cells analyzed in this study are available at <http://compbio.mit.edu/scADbbb/>. The interactive website is linked from <http://compbio2.mit.edu/scadbbb/>. ROSMAP data can be requested at <https://www.radc.rush.edu>. Raw data are available upon request from <https://www.synapse.org/#!Synapse:syn51015750>.

Code availability

The code used in this study is available at <http://compbio.mit.edu/scADbbb/> and <https://github.com/nasunmit/scadbbb>.

References

59. Bennett, D. A. et al. Religious orders study and rush memory and aging project. *J. Alzheimers Dis.* **64**, S161–S189 (2018).
60. Bennett, D. A. et al. Natural history of mild cognitive impairment in older persons. *Neurology* **59**, 198–205 (2002).
61. Bennett, D. A. et al. Apolipoprotein E ϵ 4 allele, AD pathology, and the clinical expression of Alzheimer's disease. *Neurology* **60**, 246–252 (2003).
62. Bennett, D. A. et al. Neuropathology of older persons without cognitive impairment from two community-based studies. *Neurology* **66**, 1837–1844 (2006).
63. Bennett, D. A., Schneider, J. A., Wilson, R. S., Bienias, J. L. & Arnold, S. E. Neurofibrillary tangles mediate the association of amyloid load with clinical Alzheimer disease and level of cognitive function. *Arch. Neurol.* **61**, 378–384 (2004).
64. Bennett, D. A. et al. Decision rules guiding the clinical diagnosis of Alzheimer's disease in two community-based cohort studies compared to standard practice in a clinic-based cohort study. *Neuroepidemiology* **27**, 169–176 (2006).
65. Mathys, H. et al. Single-cell transcriptomic analysis of Alzheimer's disease. *Nature* **570**, 332–337 (2019).
66. Zheng, G. X. Y. et al. Massively parallel digital transcriptional profiling of single cells. *Nat. Commun.* **8**, 14049 (2017).
67. Hao, Y. et al. Integrated analysis of multimodal single-cell data. *Cell* **184**, 3573–3587 (2021).
68. Korsunsky, I. et al. Fast, sensitive and accurate integration of single-cell data with Harmony. *Nat. Methods* **16**, 1289–1296 (2019).
69. McGinnis, C. S., Murrow, L. M. & Gartner, Z. J. DoubletFinder: doublet detection in single-cell RNA sequencing data using artificial nearest neighbors. *Cell Syst.* **8**, 329–337 (2019).
70. Wang, D. et al. Comprehensive functional genomic resource and integrative model for the human brain. *Science* **362**, eaat8464 (2018).
71. Finak, G. et al. MAST: a flexible statistical framework for assessing transcriptional changes and characterizing heterogeneity in single-cell RNA sequencing data. *Genome Biol.* **16**, 278 (2015).
72. Robinson, M. D., McCarthy, D. J. & Smyth, G. K. edgeR: a Bioconductor package for differential expression analysis of digital gene expression data. *Bioinformatics* **26**, 139–140 (2010).
73. Bankhead, P. et al. QuPath: open source software for digital pathology image analysis. *Sci. Rep.* **7**, 16878 (2017).
74. Chen, E. Y. et al. Enrichr: interactive and collaborative HTML5 gene list enrichment analysis tool. *BMC Bioinformatics* **14**, 128 (2013).
75. Xie, Z. et al. Gene set knowledge discovery with Enrichr. *Curr. Protoc.* **1**, e90 (2021).
76. Kuleshov, M. V. et al. Enrichr: a comprehensive gene set enrichment analysis web server 2016 update. *Nucleic Acids Res.* **44**, W90–W97 (2016).
77. Ashburner, M. et al. Gene Ontology: tool for the unification of biology. *Nat. Genet.* **25**, 25–29 (2000).
78. The Gene Ontology Consortium. The Gene Ontology Resource: 20 years and still GOing strong. *Nucleic Acids Res.* **47**, D330–D338 (2019).
79. Jin, S. et al. Inference and analysis of cell–cell communication using CellChat. *Nat. Commun.* **12**, 1088 (2021).
80. Efremova, M., Vento-Tormo, M., Teichmann, S. A. & Vento-Tormo, R. CellPhoneDB: inferring cell–cell communication from combined expression of multi-subunit ligand–receptor complexes. *Nat. Protoc.* **15**, 1484–1506 (2020).
81. Shao, X. et al. CellTalkDB: a manually curated database of ligand–receptor interactions in humans and mice. *Brief. Bioinform.* **22**, bbaa269 (2021).
82. Cabello-Aguilar, S. et al. SingleCellSignalR: inference of intercellular networks from single-cell transcriptomics. *Nucleic Acids Res.* **48**, e55 (2020).
83. Park, Y. P. & Kellis, M. CoCoA-diff: counterfactual inference for single-cell gene expression analysis. *Genome Biol.* **22**, 228 (2021).
84. Barber, R. F. & Candès, E. J. Controlling the false discovery rate via knockoffs. *Ann. Stat.* **43**, 2055–2085 (2015).
85. Wang, Y. & Blei, D. M. The blessings of multiple causes. *J. Am. Stat. Assoc.* **114**, 1574–1596 (2019).
86. Zhu, Z., Fan, Y., Kong, Y., Lv, J. & Sun, F. DeepLINK: deep learning inference using knockoffs with applications to genomics. *Proc. Natl Acad. Sci. USA* **118**, e2104683118 (2021).
87. Jiang, T., Li, Y. & Motsinger-Reif, A. A. Knockoff boosted tree for model-free variable selection. *Bioinformatics* **37**, 976–983 (2021).
88. Candès, E., Fan, Y., Janson, L. & Lv, J. Panning for gold: 'model-X' knockoffs for high dimensional controlled variable selection. *J. R. Stat. Soc. Series B Stat. Methodol.* **80**, 551–577 (2018).
89. Kaul, A., Bhattacharyya, S. & Ay, F. Identifying statistically significant chromatin contacts from Hi-C data with FitHiC2. *Nat. Protoc.* **15**, 991–1012 (2020).
90. Lalonde, S. et al. Integrative analysis of vascular endothelial cell genomic features identifies AIDA as a coronary artery disease candidate gene. *Genome Biol.* **20**, 133 (2019).
91. Niskanen, H. et al. Endothelial cell differentiation is encompassed by changes in long range interactions between inactive chromatin regions. *Nucleic Acids Res.* **46**, 1724–1740 (2018).
92. Mumbach, M. R. et al. Enhancer connectome in primary human cells identifies target genes of disease-associated DNA elements. *Nat. Genet.* **49**, 1602–1612 (2017).
93. Boix, C. A., James, B. T., Park, Y. P., Meuleman, W. & Kellis, M. Regulatory genomic circuitry of human disease loci by integrative epigenomics. *Nature* **590**, 300–307 (2021).
94. Aguet, F. et al. The GTEx Consortium atlas of genetic regulatory effects across human tissues. *Science* **369**, 1318–1330 (2020).

Acknowledgements

We thank the study participants and staff of the Rush Alzheimer's Disease Center. This work was supported in part by National Institutes of Health grant nos. AG054012, AG058002, AG062377, NS110453, NS115064, AG062335 and NS127187 (M.K., L.-H.T.); grant nos. AG067151, MH109978, MH119509, HG008155 and DA053631 (M.K.); grant nos. P3OAG10161, P3OAG72975, R01AG15819, R01AG17917, U01AG46152, U01AG61356 and R01AG57473 (D.A.B.); and the Cure Alzheimer's Foundation CIRCUITS consortium (M.K., L.-H.T.); the JPB Foundation (L.-H.T.); and Robert A. and Renee Belfer (L.-H.T.). N.S. was supported by a Takeda Fellowship from the Takeda Pharmaceutical Company. We thank C. A. Boix, L. Hou, A. Grayson and P. Purcell for scientific suggestions.

Author contributions

N.S., M.K. and L.-H.T. conceived and designed the study. M.K. and L.-H.T. supervised the study. N.S. developed the computational framework and conducted the data analysis with assistance from

Y.P., H.M. and K.G. X.J. and A.P.N. performed the snRNA-seq profiling. L.A.A., M.H.M. and F.G.-M. performed the in situ hybridization and quantification with help from A.B. D.A.B. provided the postmortem samples and scientific input. N.S. and M.K. wrote the paper with comments from all authors.

Competing interests

The authors declare no competing interests.

Additional information

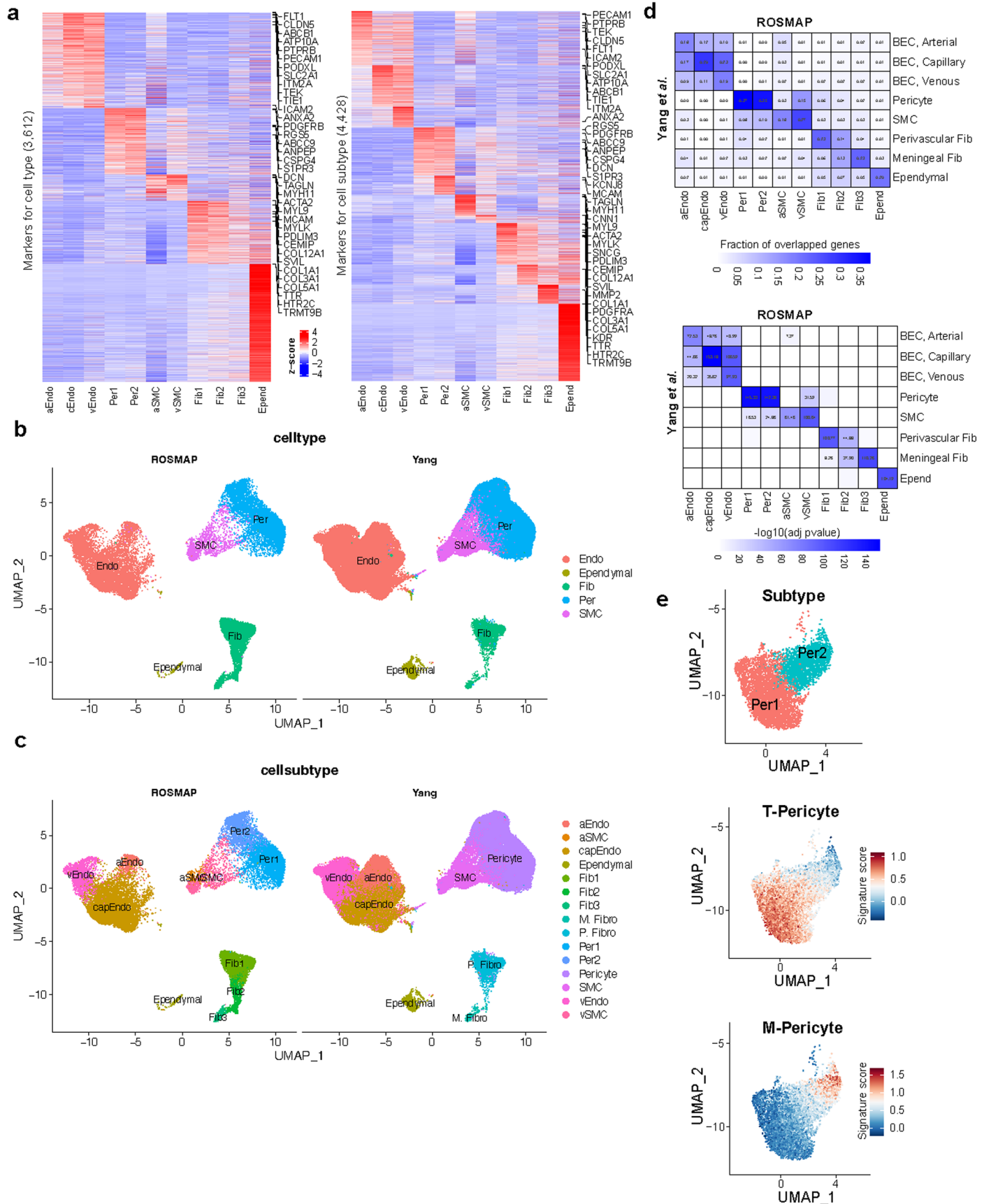
Extended data is available for this paper at <https://doi.org/10.1038/s41593-023-01334-3>.

Supplementary information The online version contains supplementary material available at <https://doi.org/10.1038/s41593-023-01334-3>.

Correspondence and requests for materials should be addressed to Li-Huei Tsai or Manolis Kellis.

Peer review information *Nature Neuroscience* thanks Nancy Ip and the other, anonymous, reviewer(s) for their contribution to the peer review of this work.

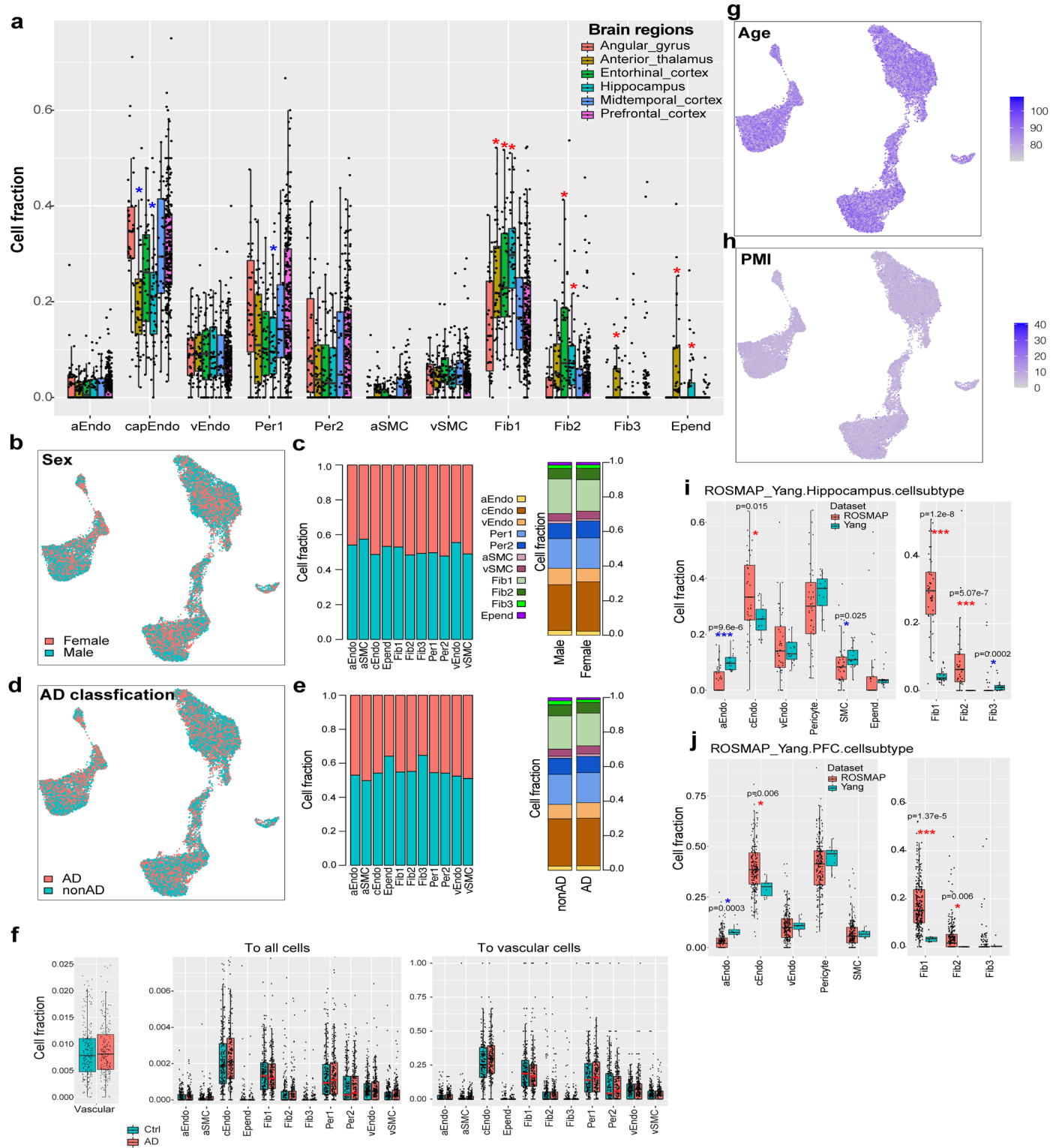
Reprints and permissions information is available at www.nature.com/reprints.



Extended Data Fig. 1 | See next page for caption.

Extended Data Fig. 1 | Brain vasculature characterization across six brain regions. a. Markers for vascular cell types (left) and cell subtypes (right). The z-scores are shown at the pseudo-bulk level. The top 5 markers for each cell type or subtype with highest fold change and the known markers are shown along the right side of the heatmap. **b-c.** UMAPs showing the comparison of brain vascular nuclei in this study (labeled as 'ROSMAP') and Yang *et al.* at both the cell type (b) and subtype (c) levels. **d.** Heatmaps showing the significant overlap of marker genes at the subtype level between this study (labeled as 'ROSMAP') and Yang *et al.* (top: significance; bottom: the fraction of overlapped genes). The

top heatmap shows the fraction of overlapped genes. The $-\log_{10}(\text{adj. p-value})$ are shown in the bottom heatmap to represent the significance (Fisher's exact test, two-sided adjusted p-value < 0.05 as a cutoff). **e.** UMAPs showing the correspondence of pericyte subtypes between this study and Yang *et al.* The top UMAP shows the two subtypes of pericytes identified in this study. The bottom two UMAPs show the T-pericyte and M-pericyte signature score distribution in this study. The signature genes of T-pericyte and M-pericyte were defined in Yang *et al.*



Extended Data Fig. 2 | See next page for caption.

Extended Data Fig. 2 | Cell fraction analysis. **a.** Distribution of cell fraction across six brain regions in cell subtypes. The stars represent the significance of cell types enriched (red star) or depleted (blue star) in specific regions compared to the overall fraction by the Wilcoxon rank test adjusted p-value < 0.05. n = 409 in PFC; 47 in angular gyrus, mid-temporal cortex and thalamus; 45 in entorhinal cortex; 84 in hippocampus. The box starts in the first quantile (25%) and ends in the third (75%). The line inside represents the median. Two whiskers represent the maximum and minimum without outliers. **b-c.** Cerebrovascular cell distribution by sex. **b.** UMAP of brain vascular nuclei colored by sex. **c.** Cell fraction across sex for each cell type (**left**) and across cell types for male and female individuals (**right**). **d-e.** Cerebrovascular cell distribution by AD classification. **d.** UMAP of brain vascular nuclei colored by AD classification. **e.** Cell fraction across AD classification for each cell type (**left**) and across cell types for AD and control individuals (**right**). **f.** Cell fraction distribution between control and AD

individuals in overall vascular cells (**left**) and each cell type (**middle**: in all cells; **right**: in vascular cells) (n = 220 for AD and n = 208 for nonAD). The box starts in the first quantile (25%) and ends in the third (75%). The line inside represents the median. Two whiskers represent the maximum and minimum without outliers. **g-h.** UMAP of brain vascular nuclei colored by age (g) and PMI (h) showing no difference of cell distribution with age or PMI. **i-j.** Comparison of cell fraction between this study (labeled 'ROSMAP') and Yang *et al.* in hippocampus (i) and prefrontal cortex (j). Stars represent the statistical significance by the Wilcoxon rank test (*: adjusted p-value < 0.05, ***: adjusted p-value < 0.001). Blue stars indicate a higher fraction in Yang *et al.* and red stars represent a higher fraction in this study. For hippocampus, n = 42 for ROSMAP data, n = 17 for Yang *et al.* data; for PFC, n = 233 for ROSMAP data, n = 8 for Yang *et al.* data. The box starts in the first quantile (25%) and ends in the third (75%). The line inside represents the median. Two whiskers represent the maximum and minimum without outliers.



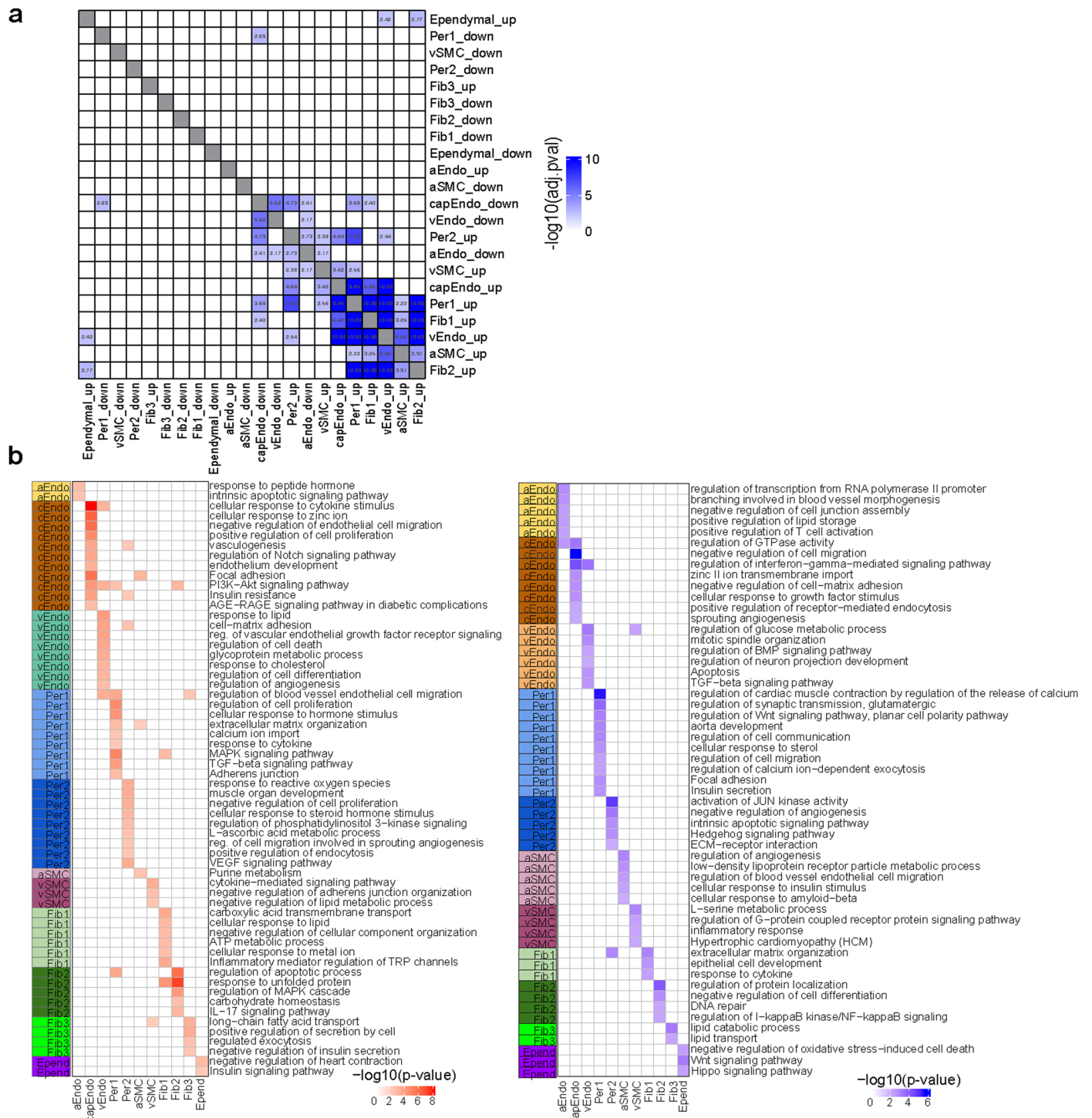
Extended Data Fig. 3 | Differential gene analysis across brain regions.
a. Heatmap of the number of highly expressed brDEGs in each region and for each cell type. The intensity of the color corresponds to the quantity of brDEGs (indicated in each cell). **b.** Enriched Gene Ontology biological processes in each

cell type. Heatmap of -log10(p-value) indicates the significance. Enrichr in R was used to perform GO enrichment (proportion test, adjusted p-value < 0.05 as cutoff, one-sided). Only regions with enriched terms were kept.

Extended Data Fig. 4 | Cell-type-specific brain vasculature changes in AD.

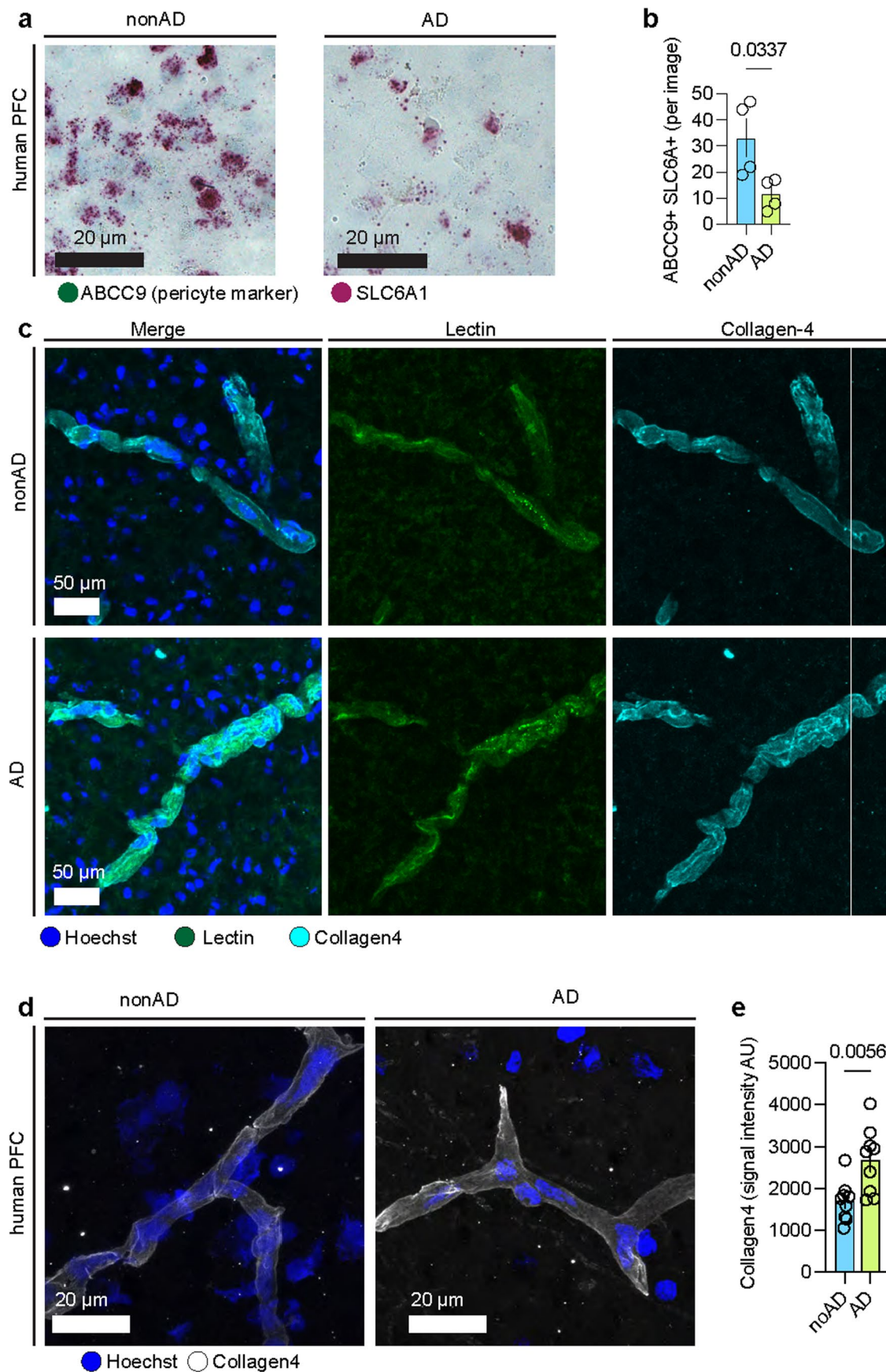
a. The distribution of numbers of adDEGs in permutation and real analysis. The adDEGs were identified based on permuted AD classification for each individual, and the p-value was estimated by t-test. $n = 428$ individuals for permutation analysis. The box starts in the first quantile (25%) and ends in the third (75%). The line inside represents the median. Two whiskers represent the maximum and minimum without outliers. **b.** Heatmaps of the consistency of adDEGs using single-cell based (MAST) and pseudo-bulk based (edgeR) methods. The fraction of overlapped genes is shown in the top heatmap. The $-\log_{10}(\text{adj. p-value})$ by Fisher's exact test represents the significance and is shown in the bottom heatmap (two-sided). **c.** The consistency of adDEGs in cEndo using different

numbers of cells by downsampling analysis (1000, 2000, 3000, 4000, 5000 and the original 6195 cEndo cells). For each panel, the x-axis represents the significance of adDEGs in the downsampling condition listed at the top of the columns. The significance was measured by $\log(\text{p-value})$, and the sign indicates the direction of effect size in this condition. The y-axis shows the effect size in the downsampling condition listed at the right of the rows. The effect size was measured by coefficient in MAST. **d.** Comparison of adDEGs across brain regions in each cell type. Each heatmap shows the significant overlap of adDEGs between brain regions in one cell type. Significance represented by $-\log_{10}(\text{adj. p-value})$ by Fisher's exact test (two-sided). Six cell types with enough cells to identify adDEGs in each region are included in this analysis.



Extended Data Fig. 5 | Functional enrichment of adDEGs. a. Heatmap showing the significance of GO term overlap between adDEG sets. The $-\log_{10}(\text{adj.p-value})$ by Fisher's exact test represents the significance ($\text{adj.p-value} < 0.05$ as a cutoff). **b.** Top enriched Gene Ontology biological processes in up-regulated adDEGs

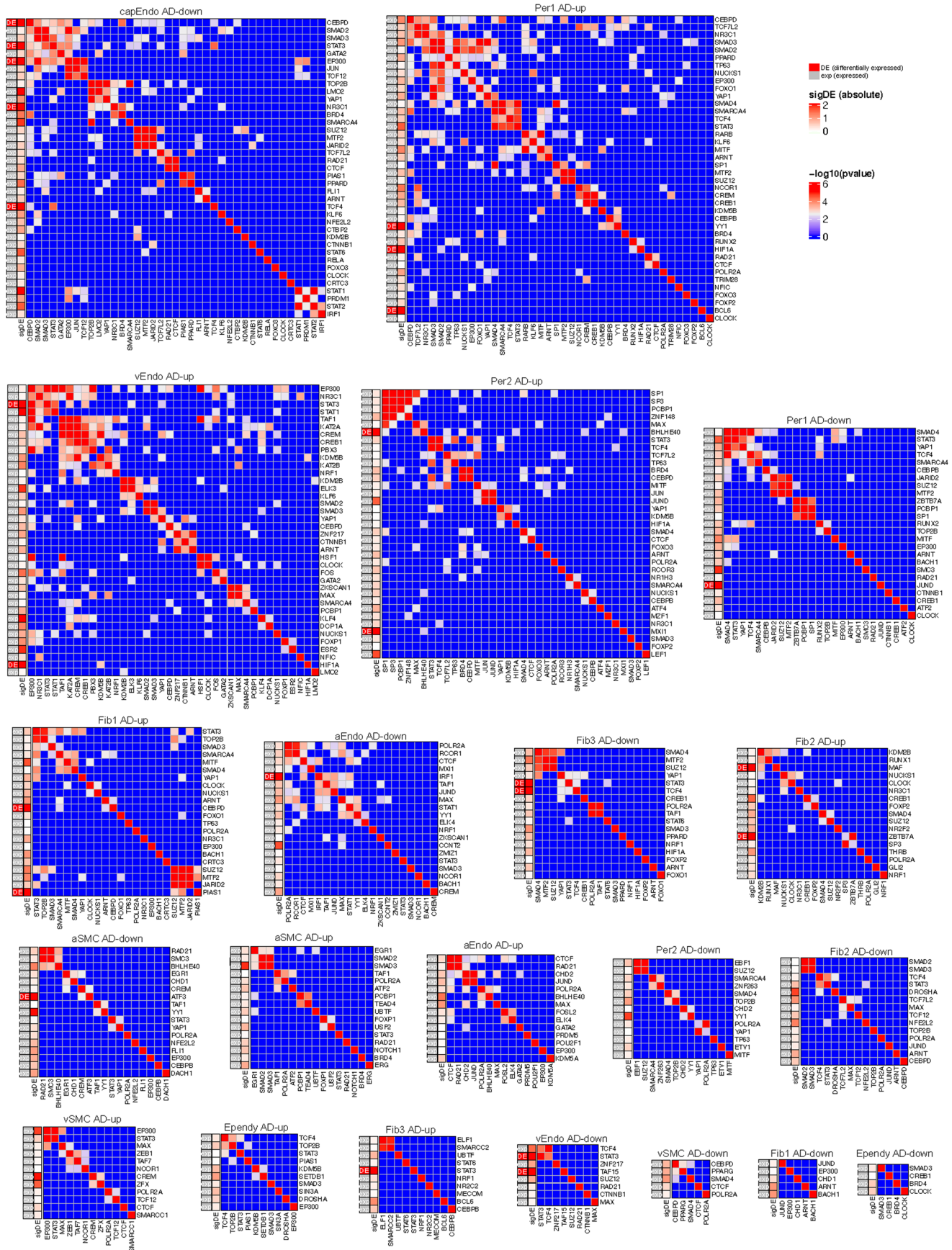
(left) and down-regulated adDEGs (right). Enrichr in R was used to perform GO enrichment (proportion test, adjusted p-value < 0.05 as cutoff, one-sided). The full list of enriched GO terms is shown in Supplementary Table 7.



Extended Data Fig. 6 | See next page for caption.

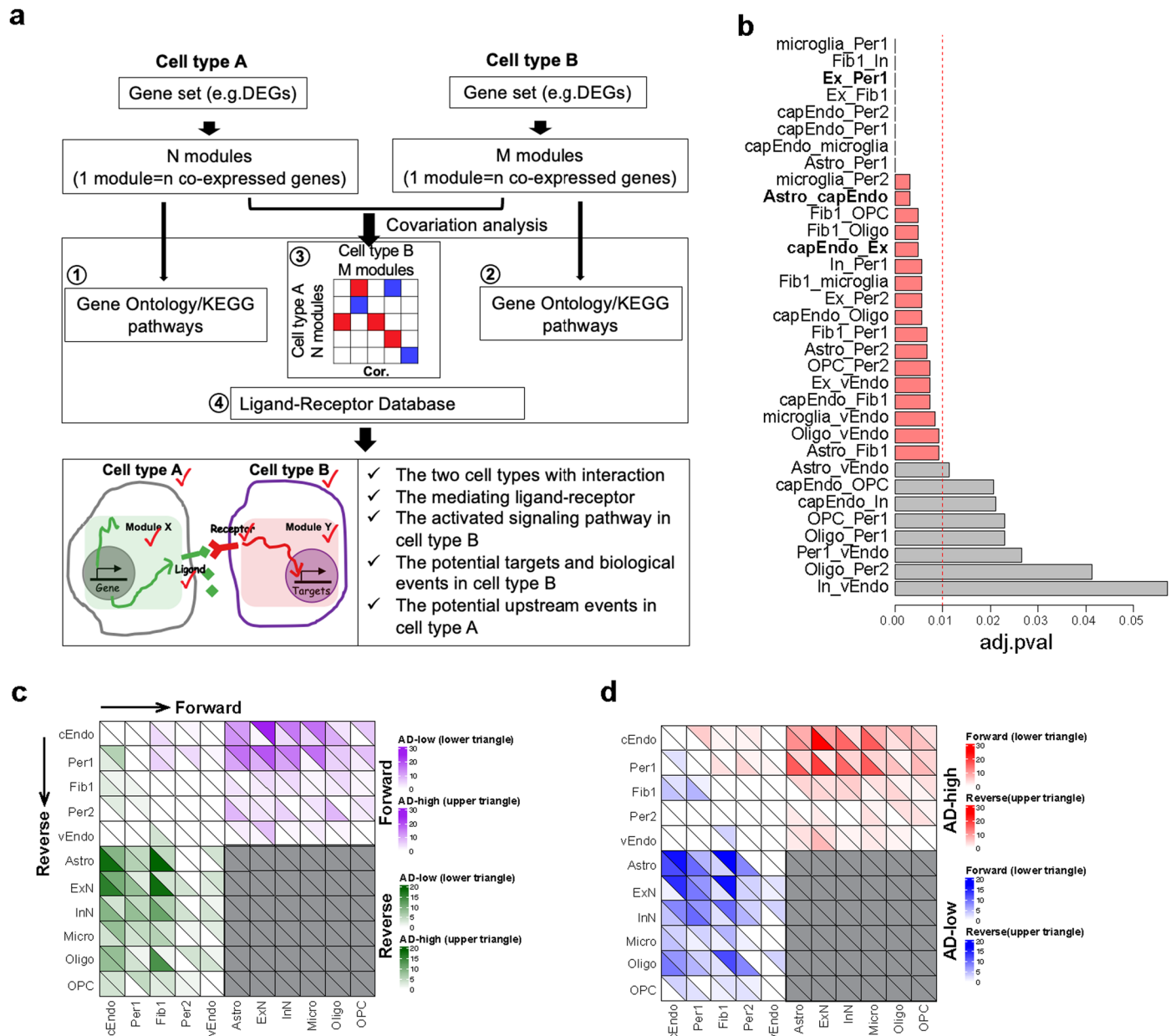
Extended Data Fig. 6 | Experimental validation of adDEGs. **a.** Chromogenic RNAscope for ABCC9 and SLC6A1. Prefrontal cortex brain sections (n = 4 for AD and n = 4 for nonAD) were sectioned at 20 μm (3 images per slide), then stored at -80°C . Sections were then prepared for RNAscope using the manufacturer's instructions. Scale bar, 20 μm . **b.** Quantification of SLC6A and ABCC9 double-positive cells per image. P value was calculated by t-test. Data are

presented as mean values \pm standard deviation. **c.** Collagen-4 and lectin-488 immunohistochemistry. Scale bar, 50 μm . **d.** Additional images of collagen-4 immunohistochemistry. Scale bar, 20 μm . **e.** Quantification of collagen-4 signal intensity. P value was calculated by t-test (n = 4 for AD and n = 4 for nonAD individuals). Data are presented as mean values \pm standard deviation.



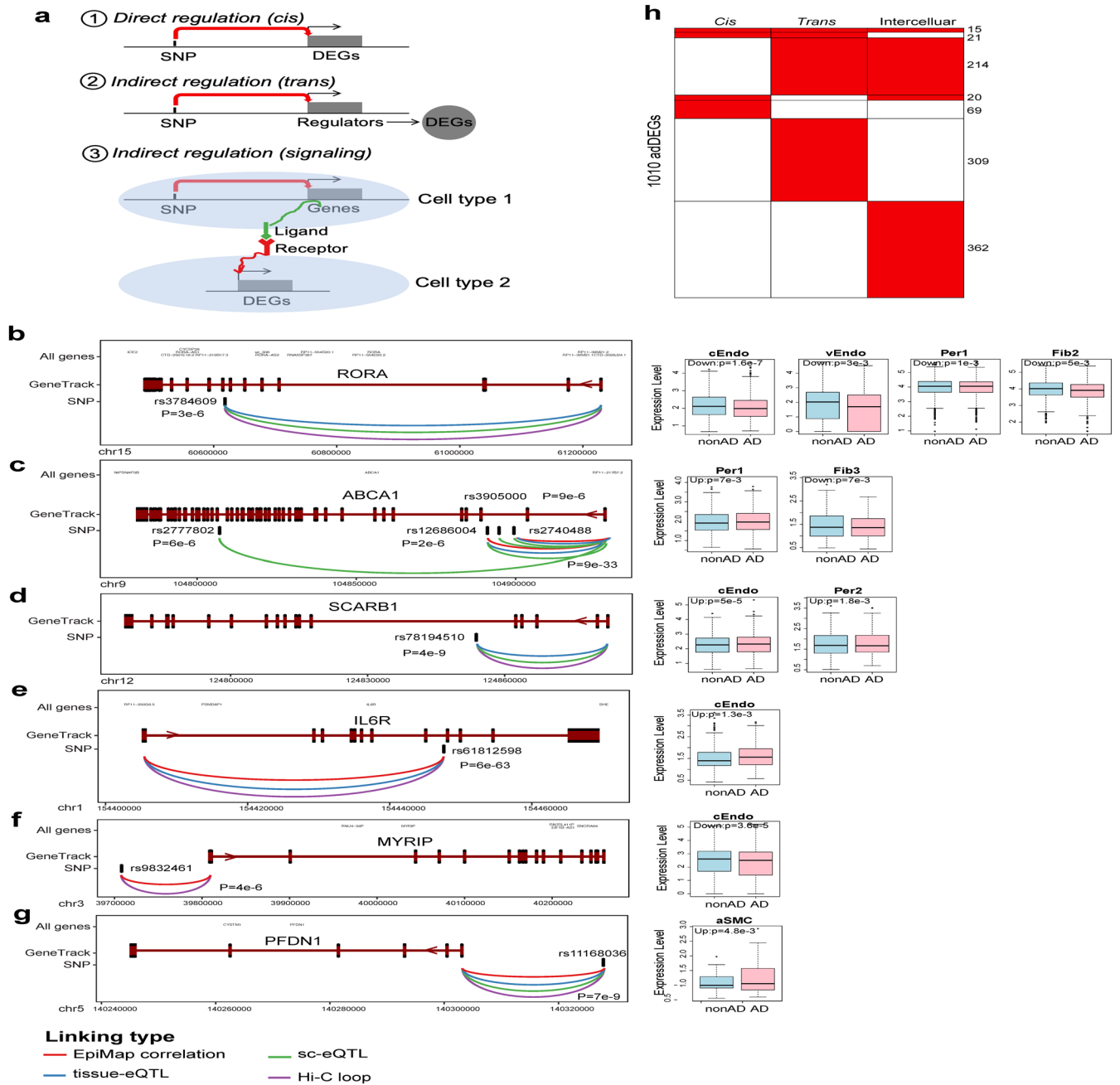
Extended Data Fig. 7 | Upstream regulators of adDEGs. Regulator modules of adDEGs in 11 cell types. On the left of each heatmap, the first column shows if the regulator is significantly differentially expressed (adDEGs, labeled as DE) or just expressed (exp) in the corresponding cell type. The second column shows

the significance of differential expression as represented by the coefficient calculated in MAST analysis. The heatmap shows $-\log_{10}(\text{p-value})$ to represent the significance of overlapping targets between regulators by Fisher's exact test (two-sided).



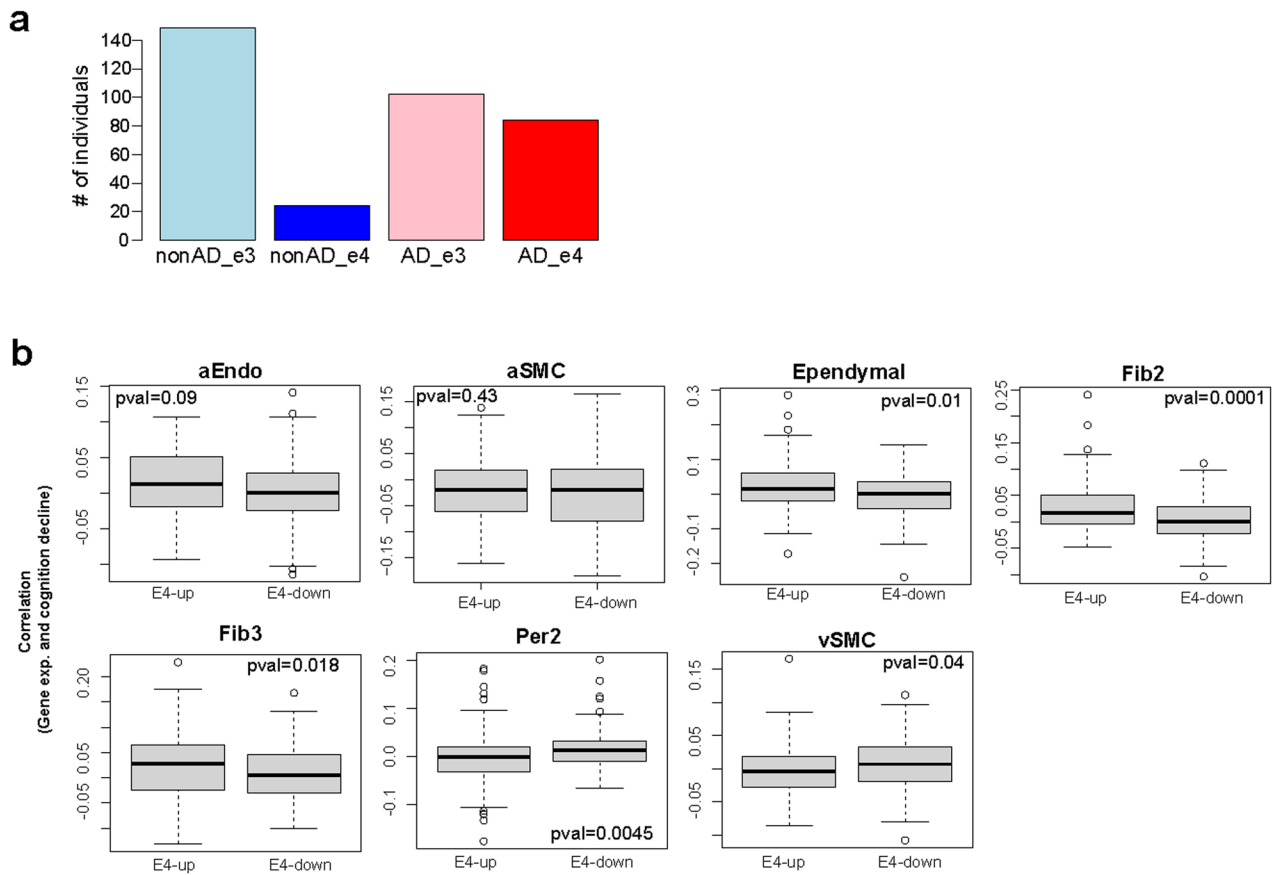
Extended Data Fig. 8 | Dynamics of cell-cell communications between vascular cell types and neuron/glia cells in AD. a. Computational framework to infer cell-cell communications. For each cell type, a set of genes was clustered into a number of co-expressed modules. The pairwise Pearson correlation coefficient was calculated between modules for each pair of cell types. The significantly correlated modules, functional enrichment, and ligand-receptor pairs were integrated into the prediction of cell-cell communication. The output includes the interacting cell types, ligand, ligand-involved functions, receptor, receptor-involved functions, potential targets in signal receiver cell type, and direction of cell-cell communication (as determined by the changes of ligand-receptor and their co-expressed genes in the same module) in AD. **b.** Bar plot showing the statistical significance of the cell-cell communications, as represented by the adjusted p-value using a permutation test in each pair of interacting cell types. An adjusted p-value of 0.01 (dashed line) was used as a cutoff. The three cell pairs which had the most cell-cell communication (Ex_Per1, Astro_cEndo and cEndo_Ex) are highlighted in bold. **c.** Heatmap showing the up- and down-regulation of both forward and reverse cell-cell communications

in AD. The purple indicates the number of forward interactions (from cell type on the left of the plot to cell type on the bottom of the plot) that were upregulated in AD (upper triangle in each square) and downregulated in AD (lower triangle in each square). The green indicates the number of reverse interactions (from the cell type on the bottom of the plot to the cell type on the left of the plot) that were upregulated in AD (upper triangle in each square) and downregulated in AD (lower triangle in each square). **d.** Heatmap showing the forward and reverse cell-cell communications that are both up- and down-regulated in AD. The red indicates the number of upregulated interactions in AD that are forward interactions (from cell type on the left of the plot to cell type on the bottom of the plot, lower triangle) and reverse interactions (from the cell type on the bottom of the plot to the cell type on the left of the plot, upper triangle). The blue indicates the number of downregulated interactions in AD that are forward interactions (from cell type on the left of the plot to cell type on the bottom of the plot, lower triangle) and reverse interactions (from the cell type on the bottom of the plot to the cell type on the left of the plot, upper triangle).



Extended Data Fig. 9 | AD GWAS loci linked to brain vascular adDEGs. a. Three proposed types of regulatory mechanisms to interpret the association between adDEGs and AD genetic variants: (1) SNP directly (*cis*) regulates adDEG; (2) SNP indirectly (*trans*) regulate adDEG; (3) SNP indirectly (*ligand-receptor signaling*) regulates adDEG. **b-g.** Examples of adDEGs directly regulated by AD-associated variants through linking (eQTLs, Hi-C, promoter-enhancer correlation) along with the expression changes in vascular cell types in AD shown in the boxplots

on the right ($n = 10,272$ and $12,242$ nuclei in AD and control individuals). The box starts in the first quantile (25%) and ends in the third (75%). The line inside represents the median. Two whiskers represent the maximum and minimum without outliers. Likelihood ratio test is used here (two-sided, adjusted p -value < 0.05 as cutoff. P -value is shown in the barplot.). **h.** The number of targets regulated by three, two, or only one of the regulatory mechanisms.



Extended Data Fig. 10 | APOE4-associated DEGs and cognitive decline.

a. The number of individuals with each combination of AD classification and APOE genotype: nonAD with ϵ 33 alleles, nonAD with ϵ 4 allele, AD with ϵ 33 alleles,

and AD with ϵ 4 allele. **b.** The comparison of apoeDEGs correlation with cognitive decline between up-regulated and down-regulated apoeDEGs in the APOE4 group in each cell type.

Reporting Summary

Nature Portfolio wishes to improve the reproducibility of the work that we publish. This form provides structure for consistency and transparency in reporting. For further information on Nature Portfolio policies, see our [Editorial Policies](#) and the [Editorial Policy Checklist](#).

Statistics

For all statistical analyses, confirm that the following items are present in the figure legend, table legend, main text, or Methods section.

n/a Confirmed

- | | | |
|-------------------------------------|-------------------------------------|--|
| <input type="checkbox"/> | <input checked="" type="checkbox"/> | The exact sample size (n) for each experimental group/condition, given as a discrete number and unit of measurement |
| <input type="checkbox"/> | <input checked="" type="checkbox"/> | A statement on whether measurements were taken from distinct samples or whether the same sample was measured repeatedly |
| <input type="checkbox"/> | <input checked="" type="checkbox"/> | The statistical test(s) used AND whether they are one- or two-sided
<i>Only common tests should be described solely by name; describe more complex techniques in the Methods section.</i> |
| <input type="checkbox"/> | <input checked="" type="checkbox"/> | A description of all covariates tested |
| <input type="checkbox"/> | <input checked="" type="checkbox"/> | A description of any assumptions or corrections, such as tests of normality and adjustment for multiple comparisons |
| <input type="checkbox"/> | <input checked="" type="checkbox"/> | A full description of the statistical parameters including central tendency (e.g. means) or other basic estimates (e.g. regression coefficient) AND variation (e.g. standard deviation) or associated estimates of uncertainty (e.g. confidence intervals) |
| <input type="checkbox"/> | <input checked="" type="checkbox"/> | For null hypothesis testing, the test statistic (e.g. F , t , r) with confidence intervals, effect sizes, degrees of freedom and P value noted
<i>Give P values as exact values whenever suitable.</i> |
| <input checked="" type="checkbox"/> | <input type="checkbox"/> | For Bayesian analysis, information on the choice of priors and Markov chain Monte Carlo settings |
| <input checked="" type="checkbox"/> | <input type="checkbox"/> | For hierarchical and complex designs, identification of the appropriate level for tests and full reporting of outcomes |
| <input type="checkbox"/> | <input checked="" type="checkbox"/> | Estimates of effect sizes (e.g. Cohen's d , Pearson's r), indicating how they were calculated |

Our web collection on [statistics for biologists](#) contains articles on many of the points above.

Software and code

Policy information about [availability of computer code](#)

Data collection

Data analysis

For manuscripts utilizing custom algorithms or software that are central to the research but not yet described in published literature, software must be made available to editors and reviewers. We strongly encourage code deposition in a community repository (e.g. GitHub). See the Nature Portfolio [guidelines for submitting code & software](#) for further information.

Data

Policy information about [availability of data](#)

All manuscripts must include a [data availability statement](#). This statement should provide the following information, where applicable:

- Accession codes, unique identifiers, or web links for publicly available datasets
- A description of any restrictions on data availability
- For clinical datasets or third party data, please ensure that the statement adheres to our [policy](#)

Human research participants

Policy information about [studies involving human research participants and Sex and Gender in Research](#).

Reporting on sex and gender

All information about human individuals is included in Supplementary Table 1.

Population characteristics

Human research participants are gender balanced and 85 years old on average. Quantitative clinical and pathologic phenotypes of AD were used to assess disease severity. These included global cognition proximate to death, and a measure of global AD pathology as well as the molecularly specific beta-amyloid and PHFtau tangles. Specifically, we performed k-means clustering on this quantitative matrix after z-score normalization to group all patients in the cohort into k=3 clusters: non-AD (controls), early-AD, and late-AD (Supplementary Fig. 1a). Controls were defined as individuals with little to no AD pathology, whereas cases (early- and late-AD) included a spectrum of AD pathology. Thus, case status was based solely based on AD pathology and other variables were allowed to freely associate. All covariates are included in Supplementary Table 1.

Recruitment

Human brain tissues in this study were obtained from the Religious Orders Study and Rush Memory and Aging Project (ROSMAP)

Ethics oversight

Institutional Review Board (IRB) of Rush University Medical Center

Note that full information on the approval of the study protocol must also be provided in the manuscript.

Field-specific reporting

Please select the one below that is the best fit for your research. If you are not sure, read the appropriate sections before making your selection.

Life sciences Behavioural & social sciences Ecological, evolutionary & environmental sciences

For a reference copy of the document with all sections, see [nature.com/documents/nr-reporting-summary-flat.pdf](https://www.nature.com/documents/nr-reporting-summary-flat.pdf)

Life sciences study design

All studies must disclose on these points even when the disclosure is negative.

Sample size

We profiled the prefrontal cortex for 409 individuals, and four other regions for a subset of 48 individuals, including mid-temporal cortex, angular gyrus, entorhinal cortex, thalamus, as well as hippocampus for a subset of 65 individuals and an additional 19 individuals (Supplementary Table 1). We have 455 samples in PFC including 364 individuals with 1 sample, 44 individuals with 2 samples, and 1 individual with 3 samples. For other regions, there was one sample per individual (47 in angular gyrus, mid-temporal cortex and thalamus; 45 in entorhinal cortex; 84 in hippocampus). Thus, we totally have 725 samples from 428 individuals. The sample size calculation was not performed before the study. Based on the previous studies (Zimmerman et al. 2021, PMID: 33531494; Soneson et al., 2018, PMID: 29481549), we found that n=100 individuals and 24 cells per phenotypic group are high enough to detect differentially expressed genes with high power, which suggests that the numbers of samples and cells in this study are sufficient.

Data exclusions

The cells with low number of expressed genes and the doublet potential were removed from the final version of data using doublet detector algorithms.

Replication

The downsampling analysis was performed to verify the reproducibility of detecting differentially expressed genes between AD and controls. We also applied different computational methods to validate the detected DEGs. For experimental validation, we used four samples per group as biological replicates.

Randomization

The individuals between AD and controls were selected to match age, sex and PMI distributions, so it's not randomly chosen. These covariates and other relevant covariates including race, batch, and brain region, were controlled in the computational model to detect phenotype-related changes in the study.

Blinding

Blinding was not used in this study since we needed to balance the AD and control samples in different sequencing batches. In the computational analysis, we followed the same pipeline and standard to do quality control and used the phenotype information to identify differential signals.

Reporting for specific materials, systems and methods

We require information from authors about some types of materials, experimental systems and methods used in many studies. Here, indicate whether each material, system or method listed is relevant to your study. If you are not sure if a list item applies to your research, read the appropriate section before selecting a response.

Materials & experimental systems

n/a	Involvement in the study
<input type="checkbox"/>	<input checked="" type="checkbox"/> Antibodies
<input checked="" type="checkbox"/>	<input type="checkbox"/> Eukaryotic cell lines
<input checked="" type="checkbox"/>	<input type="checkbox"/> Palaeontology and archaeology
<input checked="" type="checkbox"/>	<input type="checkbox"/> Animals and other organisms
<input checked="" type="checkbox"/>	<input type="checkbox"/> Clinical data
<input checked="" type="checkbox"/>	<input type="checkbox"/> Dual use research of concern

Methods

n/a	Involvement in the study
<input checked="" type="checkbox"/>	<input type="checkbox"/> ChIP-seq
<input checked="" type="checkbox"/>	<input type="checkbox"/> Flow cytometry
<input checked="" type="checkbox"/>	<input type="checkbox"/> MRI-based neuroimaging

Antibodies

Antibodies used

For primary antibodies we used Anti-Collagen Type IV Antibody (Sigma-Aldrich #AB769, used at 1:125 concentration) and Lectin-488 (Vector Laboratories #DL-1174, used at 1:125 concentration). For secondary antibody, we used Goat anti-Rabbit IgG (H+L) Highly Cross-Adsorbed Secondary Antibody, Alexa Fluor™ 647 (Invitrogen Catalog # A-21245, used at 1:1000 concentration).

Validation

Detect Collagen Type IV using this Anti-Collagen Type IV Antibody validated for use in DB, ELISA, IC, IH. Tomato lectin (from *Lycopersicon esculentum*) is an effective marker of blood vessels and microglial cells in rodents. Conjugation of the lectin with a fluorophore facilitates fast, one-step detection and visualization using intravascular perfusion methods or direct application to tissue sections. Fluorescent dye-labeled tomato lectin is a valuable tool for studying rodent tumor angiogenesis, tracing neovascular development in xenograft models and brain research. DyLight 488-conjugated tomato lectin fluoresces green (emission maximum 518 nm) and has an excitation maximum at 493 nm. Inhibiting/Eluting Sugar: Chitin Hydrolysate